

# An investigation on loose cemented granular materials via DEM analyses

Mingjing Jiang · Wangcheng Zhang · Yugang Sun · Stefano Uti

Received: 23 May 2012 / Published online: 20 November 2012  
© Springer-Verlag Berlin Heidelberg 2012

**Abstract** This paper presents the results of a numerical study carried out by 2D discrete element method analyses on the mechanical behavior and strain localization of loose cemented granular materials. Bonds between particles were modeled in order to replicate the mechanical behavior observed in a series of laboratory tests performed on pairs of glued aluminum rods which can fail either in tension or shear (Jiang et al. in *Mech Mater* 55:1–15, 2012). This bond model was implemented in a DEM code and a series of biaxial compression tests employing lateral flexible boundaries were performed. The influence of bond strength and confinement levels on the mechanical behavior and on the onset of shear bands and their propagation within the specimens were investigated. Comparisons were also drawn with other bond models from the literature. A new dimensionless parameter incorporating the effects of both bond strength and confining pressure, called *BS*, was defined. The simulations show that shear strength and also dilation increase with the level of bond strength. It was found out that for increasing bond strength, shear bands become thinner and oriented along directions with a higher angle over the horizontal. It also emerged that the onset of localization coincided

with the occurrence of bond breakages concentrated in some zones of the specimens. The occurrence of strain localization was associated with a concentration of bonds failing in tension.

**Keywords** Cemented granular materials · Strain localization · Shear band · Bond failure · DEM

## 1 Introduction

Cemented granular materials, commonly found in natural and treated soils, are of great importance in geoenvironmental engineering and have attracted substantial interests in the last three decades (e.g., [5–9, 12–14, 17, 20, 21, 25, 26, 33, 37, 38, 40, 42, 43, 46, 54–56, 60, 67, 69–71]). Typical examples of this kind of material are provided by mortars, asphalts, volcanic ashes, sandstone and grouted soils. Interparticle bonds for these materials often consist of sediments such as gypsum, Portland cement and lime [20].

In general, at small strain, cemented granular materials exhibit a stiffer stress–strain response than their corresponding reconstituted states. At large strains, they exhibit strain softening and shear dilation [8, 18, 19, 38, 40]. Moreover, the experimental and numerical investigations performed by Wang and Leung [66, 67] showed that increasing the cement ratio leads to a shift of the stress–strain response from hardening to softening and of the volumetric behavior from contractive to dilative. Also Consoli et al. [6] investigated the influence of the void/cement ratio on initial stiffness and effective strength by means of both unconfined and triaxial compression tests.

Some constitutive models [69, 70] introduced the bond effect and were able to reproduce the major mechanical response of cemented granular materials. However, how the

M. Jiang (✉) · W. Zhang · Y. Sun  
Department of Geotechnical Engineering, Key Laboratory of Geotechnical and Underground Engineering of Ministry of Education, Tongji University, Shanghai 200092, China  
e-mail: mingjing.jiang@tongji.edu.cn

W. Zhang  
e-mail: zhwch@foxmail.com

Y. Sun  
e-mail: sunyugang136@163.com

S. Uti  
School of Engineering, University of Warwick, Coventry CV4 7AL, UK  
e-mail: S.Uti@warwick.ac.uk

bond strength affects the mechanical behavior and shear band formation of cemented granular materials is not yet fully understood at the micro scale, which constitutes a strong motivation for the present study.

Strain localization is a fundamental feature exhibited by cemented soils when subjected to shearing. In recent years, several theoretical, experimental and numerical works have been carried out on strain localization, mainly on uncemented granules (e.g., [11, 15, 16, 22, 34, 48, 57, 58, 62]). By means of advanced technologies, such as X-ray scanning [1, 51, 63], stereophotogrammetry [23] and particle image velocimetry [68], individual particle movements can be tracked and monitored at different strain levels. Unfortunately in case of cemented granular materials, experimental tests are still incapable of providing reliable information on the evolution of the network of bonds with loading and the spatial location of bond breaking events. This limitation constitutes another motivation for this paper.

The distinct element method (DEM), originally developed by Cundall and Strack [10], has been regarded as a powerful tool to investigate the mechanical behavior of granular materials at the micro scale. Also it has shown the ability to reproduce several features of cemented granular materials, such as enhanced shear strength and dilation [18, 38, 32, 40, 59, 67], liquefaction [72], permeability [49], and strain localization [38, 66]. However, the failure criteria adopted for the inter-grain bonds in DEM simulations are typically postulated [4, 47, 56]. An investigation on real cemented granules is essential to reveal the interaction laws of bonded granules. Delenne et al. [14] investigated the force-displacement relationship and failure condition by performing loading tests on a couple of aluminum rods glued by epoxy resin and thus derived a function in the space of the generalized force variables for the failure of bonds. Their study was based on simple loading tests (pure tension, compression, shear and torsion tests), while complex loading conditions with nonzero normal force were unavailable. Within this framework, Jiang et al. [37] performed a series of simple (tension and compression tests) and complex loading tests (shear combined with different normal forces) on pairs of aluminum rods glued by epoxy resin and derived a more rigorous empirical function for the bond failure.

This paper aims to present a comprehensive study and in-depth investigation of the influence of bond strength on the mechanical behavior and strain localization of cemented granular materials. In this paper, the experimentally derived bond failure criterion was implemented in a DEM code and simulations were run to identify the link between bond breakage due to either tension or shear failure and shear band formation as well as mapping the different features of the micromechanical behavior inside and outside shear bands which have not been investigated in previous studies.

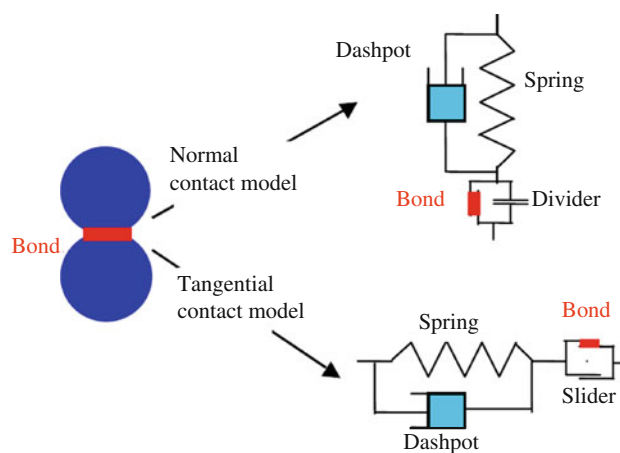


Fig. 1 Physical analogue of the employed bond models

## 2 DEM bond contact model

Jiang et al. [37] presented a comprehensive investigation on the mechanical behavior of idealized granules glued by epoxy resin, applying different kinds of forces (i.e. normal force, shear force and moment) for various combined loading paths. Two types of bond behavior were identified in their experiments, namely, the thin type and the thick one. In this paper, the employed bond model is representative of thin bonds. To speed up computations, moments (bending and torsion) acting on the bonds were neglected, with only forces considered in the bond model as shown in Fig. 1.

### 2.1 Contact stiffness

Constant normal and tangential stiffness set to  $7.5 \times 10^7$  N/m and  $5 \times 10^7$  N/m, respectively were adopted. Although the small strain-elastic stiffness of cemented soils depends on the cement content [6], the values of the contact stiffnesses,  $K_n$  and  $K_s$ , employed in the simulations were constant, since the soil elastic response at small strains was not the focus of this study. The same constant contact stiffness was employed by Wang and Leung [66, 67].

### 2.2 Bond strength criterion

Experimental data from Jiang et al. [37] showed that bonds subject to uniaxial tension behave according to a non linear brittle law (see Fig. 2a1) which was simplified into a linear elastic-brittle law for the bond model adopted in our DEM simulations (see Fig. 2a2). The tensile strength of the bonds is a material parameter here called,  $R_t$ .

In case of unbonded granular soils, the maximum shear force at contacts,  $R_{un}$ , can be calculated from the Coulomb's criterion, as:

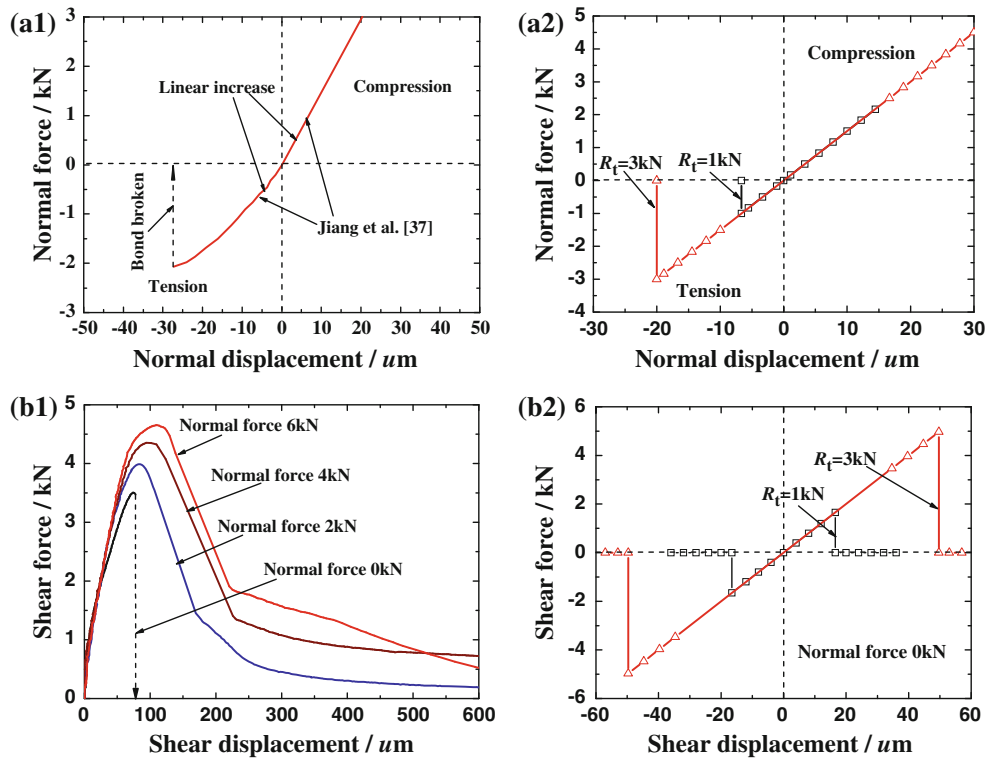


**Fig. 2** Relationship between force and displacement: **a1** experimental data in normal direction [37]; **a2** numerical bond model in the normal direction; **b1** experimental data in tangential direction [37]; **b2** numerical bond model in the tangential direction

$$R_{un} = \begin{cases} \tan \phi \cdot F_n & \text{for } F_n > 0 \\ 0 & \text{for } F_n \leq 0 \end{cases} \quad (1a,b)$$

where,  $F_n$  is the normal contact force and  $\tan \phi$  is the inter-granular friction.

Cementitious bonds are responsible for the presence of true cohesion exhibited by the bonded granular assembly at the macroscopic level and its enhanced shear strength in comparison with the case of uncemented particles (see Fig. 2b1). According to the available experimental data [37], the shear strength of a pair of bonded particles can be divided into two regions separated by a threshold value of normal force,  $F_t$  (see Fig. 3). When the normal force applied at a contact  $F_n$  is  $F_n < F_t$ , the bond adds up shear resistance  $R_s$  so that the strength envelope is curvilinear and  $R_s$  is higher than the strength for a pair of unbonded particles,  $R_{un}$ . Instead when  $F_n$  is  $F_n > F_t$ , the presence of the bond no longer increases the shear strength of the pair so that  $R_s$  coincides with  $R_{un}$ . The analytical expression for  $R_s$  is provided below:

$$R_s = \begin{cases} 1.656 \cdot R_t \cdot (1 + F_n/R_t)^{0.216} & -R_t < F_n < F_t \\ R_s = R_{un} & F_n > F_t \end{cases} \quad (2a, b)$$

It is worth noting that according to the adopted bond model, we can expect that the cohesion exhibited at the

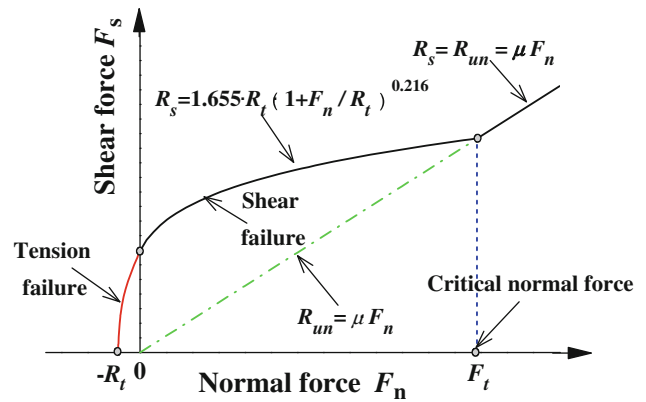


**Fig. 3** Bond strength curve in the  $F_s$ – $F_n$  plane according to the obtained experimental data [37] (colour figure online)

macroscopic level will decrease for increasing confining pressures. This bond contact model was implemented into the commercial software PFC<sup>2D</sup> [27] via a user-defined routine. The shearing force–displacement relationships for pairs of bonded particles subject to different normal forces are shown in Fig. 2a2, b2.

According to the adopted bond model, bond breakage is always brittle, i.e. a bond breaks as soon as the force acting on the bond ( $F_n, F_s$ ) reaches the strength envelope. To distinguish between tensile and shear modes, a failure has

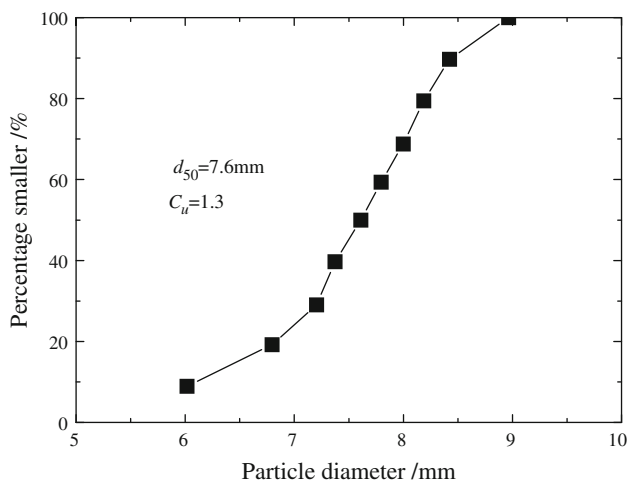


**Fig. 4** Distribution of grain sizes in DEM analyses

been considered tensile when the strength envelope is reached with a tensile normal contact force,  $F_n < 0$  (red solid line in Fig. 3); if otherwise ( $F_n > 0$ ), the failure mode is considered a shear one (black solid line in Fig. 3).

### 3 Simulation procedures

#### 3.1 Sample preparation

In this study, the sample has a dimension of 800 mm ( $W$ )  $\times$  1,680 mm ( $H$ ) and contains a total number of 24,000 particles. The particle-size distribution adopted in this study is shown in Fig. 4, with the median particle diameter  $d_{50}$  equal to 7.6 mm and the uniformity coefficient,  $C_u$ , equal to 1.3. Table 1 lists the values of parameters adopted in the simulations.

In order to generate initial homogenous samples, the multilayer under-compaction method (UCM) proposed by Jiang et al. [31] was used. In this study, eight layers of particles were generated in sequence, with each layer consisting of 3,000 particles randomly distributed into the rectangular container of 800 mm wide and 267 mm high. To achieve the target relative large planar void ratio of 0.27, the accumulated layers of particles were compacted to an intermediate void ratio which is slightly higher than the target one. Based on the under-compaction criterion [31], the intermediate void ratios for the accumulated layers were  $e_{p(1)} = 0.2895$ ,  $e_{p(1-2)} = 0.289$ ,  $e_{p(1-3)} = 0.2885$ ,  $e_{p(1-4)} = 0.2875$ ,  $e_{p(1-5)} = 0.2835$ ,  $e_{p(1-6)} = 0.281$ ,  $e_{p(1-7)} = 0.279$  and  $e_{p(1-8)} = 0.27$ . During each compaction process, the top wall was moved downward at a constant velocity of 0.5 m/s while the lateral and the bottom walls were fixed. The interparticle friction coefficient was set to 1.0 in order to achieve the relatively high intermediate void ratio and the walls were set to be frictionless.

**Table 1** Material parameters used in the DEM analyses

Parameters	Value
<b>Cemented granules</b>	
Density/( $\text{kg m}^{-3}$ )	2,600
Normal contact stiffness for test/( $\text{N m}^{-1}$ )	$7.5 \times 10^7$
Tangential contact stiffness for test/( $\text{N m}^{-1}$ )	$5.0 \times 10^7$
Tension bond strength/N	0, 0.1, 0.5, 1, 2, 3
Interparticle coefficient of friction for test	0.5
Coefficient of friction between wall and particle	0.0
Local damping coefficient	0.5
Viscous damping coefficient	0.0
<b>Membrane particles</b>	
Diameter/mm	2.0
Density/( $\text{kg m}^{-3}$ )	1,000
Bond strength in normal direction/N	$1.0 \times 10^{100}$
Bond strength in tangential direction/N	$1.0 \times 10^{100}$
Normal contact stiffness/( $\text{N m}^{-1}$ )	$3.75 \times 10^6$
Tangential contact stiffness/( $\text{N m}^{-1}$ )	$2.5 \times 10^6$

After generation, the interparticle friction coefficient was set to 0.5 and samples were consolidated one-dimensionally under a constant pressure of 12.5 kPa. After consolidation, the at rest earth pressure coefficient,  $K_0$ , turned out to be 0.57; then bonds were assigned. Following this process of generation, samples present some anisotropy of the contact network induced by the anisotropic state of stress applied during consolidation [31]. This anisotropy tends to reflect the in-situ conditions of real geomaterials (e.g. cemented sands and weak rocks).

#### 3.2 Isotropic consolidation

Lateral flexible boundaries consisting of bonded frictionless particles were employed to mimic the presence of a soft rubber membrane as originally proposed by Khun [45]. The stress controlled flexible boundary was implemented in the code according to [66,67] where the interested reader can find all the details of the implementation. As shown in [28] the use of flexible membrane boundaries allows capturing the developing shear bands with a good degree of accuracy. The top and bottom boundaries instead, consist of very stiff walls mimicking the presence of rigid platens. Samples were then subjected to an isotropic confining pressure applied to the top and bottom platens by a servo control algorithm gradually ramping up the velocity of the platens. In Fig. 5, a typical sample after consolidation is plotted.

#### 3.3 Biaxial compression

After consolidation, the sample was compressed by moving the top and the bottom platens towards each other at a

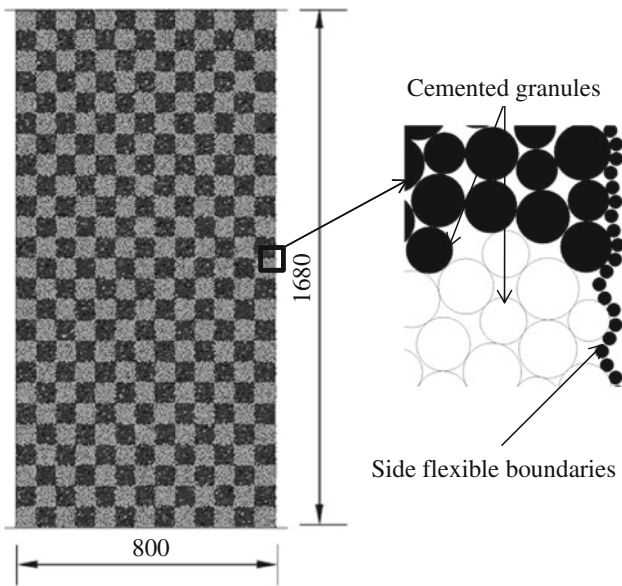


**Fig. 5** The numerical sample after consolidation in DEM analyses (unit: mm)

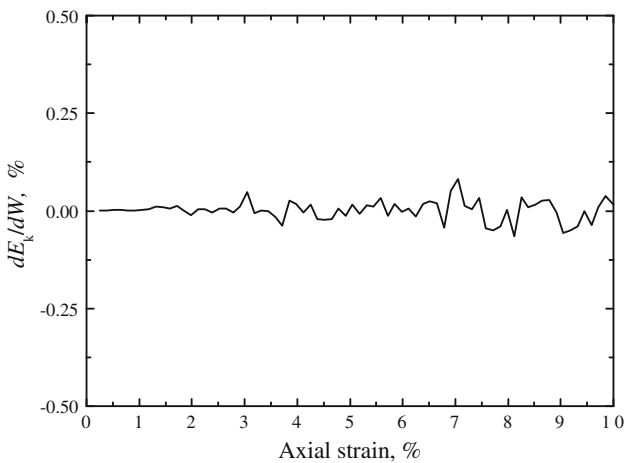


**Fig. 6** Increment of kinetic energy over the increment of external work versus axial strain ( $R_t = 1$  kN,  $\sigma_3 = 100$  kPa)

constant strain rate of 0.05 per minute while maintaining a constant pressure on the lateral flexible boundaries. The low compression rate employed here ensures that the pressure on the top and bottom platens remain close during simulations. Moreover, to ensure the presence of quasi-static conditions in the simulations, we checked the amount of kinetic energy relative to the total energy of the system. In Fig. 6, the ratio of the increment of kinetic energy over the increment of external work versus the axial strain is plotted for a typical simulation ( $R_t = 1$  kN,  $\sigma_3 = 100$  kPa). The external work represents the total energy progressively inputted in the system during loading. This ratio remains very low (0.1 %) throughout the whole simulation showing that the sample remains under quasi-static conditions.

## 4 Results and discussions

In the following sections, we report the numerical results from a series of biaxial compression tests in which the tension strength  $R_t$  ranges from 0 to 3 kN and for values of the confining pressure,  $\sigma_3$ , equal to 50, 100 and 200 kPa. In the description of the state of stress, the following 2D invariant variables have been used:  $s = (\sigma_1 + \sigma_3)/2$  (mean effective stress) and  $t = (\sigma_1 - \sigma_3)/2$  (deviatoric stress). In the description of the state of strain, the associate strain invariant variables have been used:  $\varepsilon_{vol} = \varepsilon_1 + \varepsilon_3$  (volumetric strain) and  $\varepsilon_{dev} = \varepsilon_1 - \varepsilon_3$  (deviatoric strain). This particular choice of invariants guarantees the energetic equivalence relative to the first-order work.

### 4.1 Macro mechanical properties

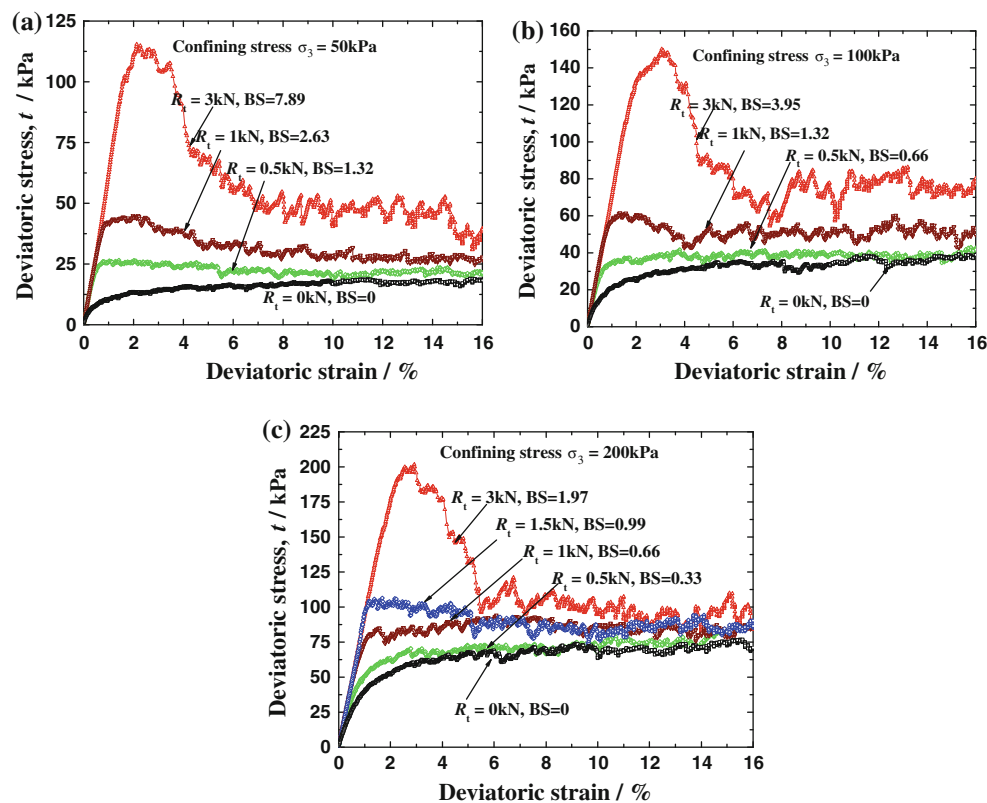
#### 4.1.1 Stress–strain relationship

Figure 7 shows the relationships between deviatoric stress and deviatoric strain obtained from three selected groups of simulations with various bond strengths,  $R_t$ , and confining pressures,  $\sigma_3$ . It is apparent that the peak deviatoric stress increases with the bond strength whatever the value of confining pressure, pointing out to a significant effect of bonds in increasing the shear strength of granular materials. Once the peak deviatoric stress is reached, the samples exhibit a strain softening branch due to the occurrence of progressively larger amounts of bonds breaking which will be illustrated later (see Fig. 17). The higher the bond strength is, the larger the amount of strain softening exhibited by the samples. Moreover, at low strains, the cemented samples show a stiffer response than the uncemented case. This is due to the fact that bonded particles are less free to rearrange than the unbonded ones [38]. These responses are in qualitative agreement with the experimental results of reference [66,67].

In addition, it can be observed that for relatively high values of confining pressure and low values of bond strength (for instance  $\sigma_3 = 200$  kPa and  $R_t = 0.5$  kN), the stress–strain response no longer exhibits strain-softening but strain hardening with the peak stress close to that of the uncemented case. From Fig. 7, we can conclude that the ratio between bond strength and confining pressure,  $R_t/\sigma_3$ , is indicative of the expected mechanical strength of the cemented assembly. In dimensionless form, we can define a normalized bond strength  $BS$  in 2D, as:

$$BS = \frac{R_t}{\sigma_3 \cdot d_{50} \cdot t} \tag{3}$$

with  $d_{50}$  the median diameter of the particle-size distribution and  $t$  the thickness of disk-like particles ( $t = 1$  in this



**Fig. 7** Stress–strain responses of cemented granular materials with different bond strengths and confinement levels: **a**  $\sigma_3 = 50$  kPa; **b**  $\sigma_3 = 100$  kPa; **c**  $\sigma_3 = 200$  kPa

study). For high values of  $BS$ , the material exhibits a marked peak in the stress–strain relationship and a strain softening branch; whereas for low values of  $BS$ , the peak lowers and the strain softening branch tends to disappear. Obviously, the response of the material tends to the one exhibited by the uncemented case for  $BS \rightarrow 0$ . At a micromechanical level, this type of response owes to the fact that at low values of  $BS$  (i.e. high confining pressures  $\sigma_3$  relative to  $R_t$ ), the average normal contact force in the assembly will be higher than the threshold  $F_t$  (see Fig. 3). When  $F_n > F_t$ , the shear strength of a bonded pair of particles coincides with the strength of an unbonded pair so that most bonds will be ineffective in increasing the macroscopic shear strength of the granular assembly.

Looking at the recorded stress–strain curves, we can also state that the value of  $BS$  rules the transition between strain-softening and strain-hardening behavior: low values of  $BS$  being associated to strain-hardening and high values to strain-softening. Looking at Fig. 7c (test run at  $\sigma = 200$  kPa) we can identify a threshold value of  $BS = 0.8$  for such a transition. However, the threshold value is likely to vary with the relative density of the sample and the particle size distribution of the granular material.

#### 4.1.2 Failure envelopes

Figure 8 provides the peak and residual strength envelopes achieved by tests run for different values of bond strength. The peak/residual internal friction angle  $\varphi_p/\varphi_r$  and the cohesion  $c$  were calculated as:

$$\sin \varphi_p = \tan a_{fp} \quad (4)$$

$$d_f = c \cos \varphi_p \quad (5)$$

$$\sin \varphi_r = \tan a_{fr} \quad (6)$$

where,  $\tan a_{fp}$  and  $\tan a_{fr}$  mean the slope of the peak and residual failure envelopes in the  $s$ – $t$  plane, and  $d_f$  denotes the intercept of the peak failure envelope.

From the figure, it emerges that the higher the adopted bond strength,  $R_t$ , is, the higher the peak internal friction angle and the macroscopic cohesion exhibited by the samples are. Although to a much less extent, an increase of the residual internal friction angle with the bond strength can be observed as well. Concerning the increase of peak friction angle and cohesion with the bond strength (see Fig. 8a), it is interesting to note that for a sufficiently high value of

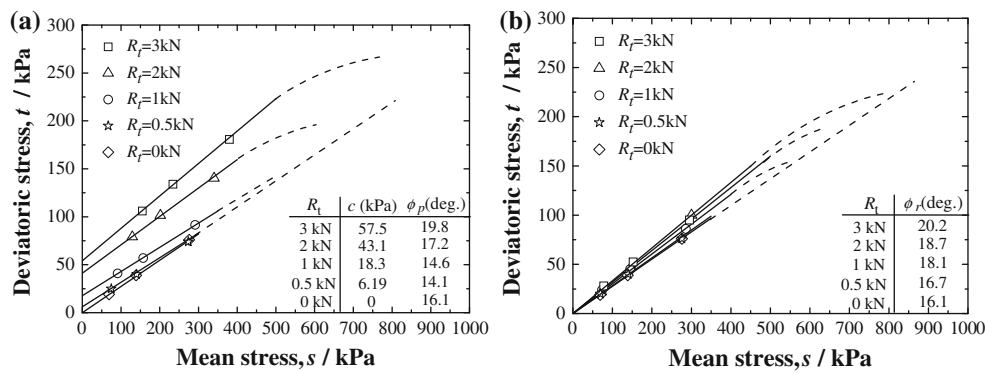


**Fig. 8** The peak and residual strength envelopes for various bond strengths: **a** peak strength envelope; **b** residual strength envelope. The stresses in this chart are spatial averages over highly non-uniform samples because of the presence of shear bands

confining pressure the strength envelopes converge to the strength envelope of the unbonded case (see the dashed lines in Fig. 8a). In fact, as pointed out by Eq. 3, progressively higher values of confining pressures translate into progressively lower values of normalized bond strength,  $BS$ , which in turn means that more and more contacts are subject to normal forces higher than the threshold value  $F_t$  implying that more and more bonds no longer provide any additional shear resistance (i.e. in Fig. 3 the branch of  $R_s$  where  $R_s = R_{un}$ ). So, according to the experimental bond model adopted, it must be expected that whatever high value of  $R_t$  is considered, at sufficiently high confining pressures, the macroscopic shear strength of the granular assembly will tend to the strength exhibited by the unbonded assembly.

An apparently curious or counterintuitive result is the fact that the peak friction angles exhibited for low values of bond strength ( $R_t = 1$  and  $0.5$  kN in the figure) are lower than the friction angle of the uncemented case. This result finds a simple explanation remembering that all the strength envelopes for cemented samples, whatever the value of  $R_t$  adopted, are curves (as indicated by the dashed lines in the figure) which must converge on the linear strength envelope of the uncemented case ( $t = s \cdot \sin \phi$ ) for a sufficiently high value of confining pressure. Indeed, the strength envelope of the cemented samples would be more accurately expressed by a non-linear strength envelope as in the case of rock materials. However, for reasons of convenience, the strength envelope for soils is traditionally expressed in soil mechanics by the linear Mohr–Coulomb criterion (i.e.  $\tau = \sigma \tan \phi + c$ ) which translate into a linear envelope in the  $s-t$  plane too. So inevitably the inclination of the Mohr–Coulomb line for cemented materials has a limited range of validity in terms of confining pressure. In other words, the inclination of the linear envelope we have taken by the least square method on the three failure points determined in the  $s-t$  plane for each value of  $R_t$ , depends on what region of the full envelope they lie on (i.e. high or low  $BS$ ). In cases of  $R_t = 1$  kN and  $R_t = 0.5$  kN, the values of relative bond strength,  $BS$ ,

are low, hence the three failure points found in the  $s-t$  plane belong to the descending part of the curve so that the inclination of the Mohr–Coulomb envelope is lower than the inclination for the uncemented case and as a consequence,  $\phi_{un} > \phi_{peak}$ . In the case of the other bond strengths considered ( $R_t = 2$  kN;  $R_t = 3$  kN) instead, the failure points belong to a different region of the full strength envelope (higher  $BS$ ) so that the least square method provides lines which are more inclined than the uncemented case (so  $\phi_{peak} > \phi_{un}$ ) since the relative bond strength of these tests is higher (or equivalently the relative confining pressure is lower).

Concerning the residual friction angle (see Fig. 8b), values higher than the uncemented case, are due to the fact that, even at large strains ( $\epsilon_a = 0.10$ ), some bonds were still intact forming clusters within the developed shear bands, providing non-negligible rolling resistance.

#### 4.1.3 Volumetric dilation

Figure 9 presents the volumetric strain versus deviatoric strain under different values of bond strength and confining pressure. Here, the positive and negative values denote compression and dilation, respectively. In general, whatever the level of confinement, the volumetric behavior switches from contractive to dilative with increasing bond strength. This trend is in agreement with the experimental data of reference [66,67]. The increase of dilation is due to the formation of particle arches within the shear bands. This in turn occurs because of the breakage of some bonds, causing the formation of clusters of bonded particles which are free to rotate, thus contributing to volumetric dilation.

Further, the dilation angle  $\Psi$ , is studied and the results are shown in Fig. 10. In this paper, the dilation angle is defined according to reference [53] as:

$$\sin \psi = \frac{d\epsilon_1 + d\epsilon_3}{d\epsilon_1 - d\epsilon_3} \tag{7}$$

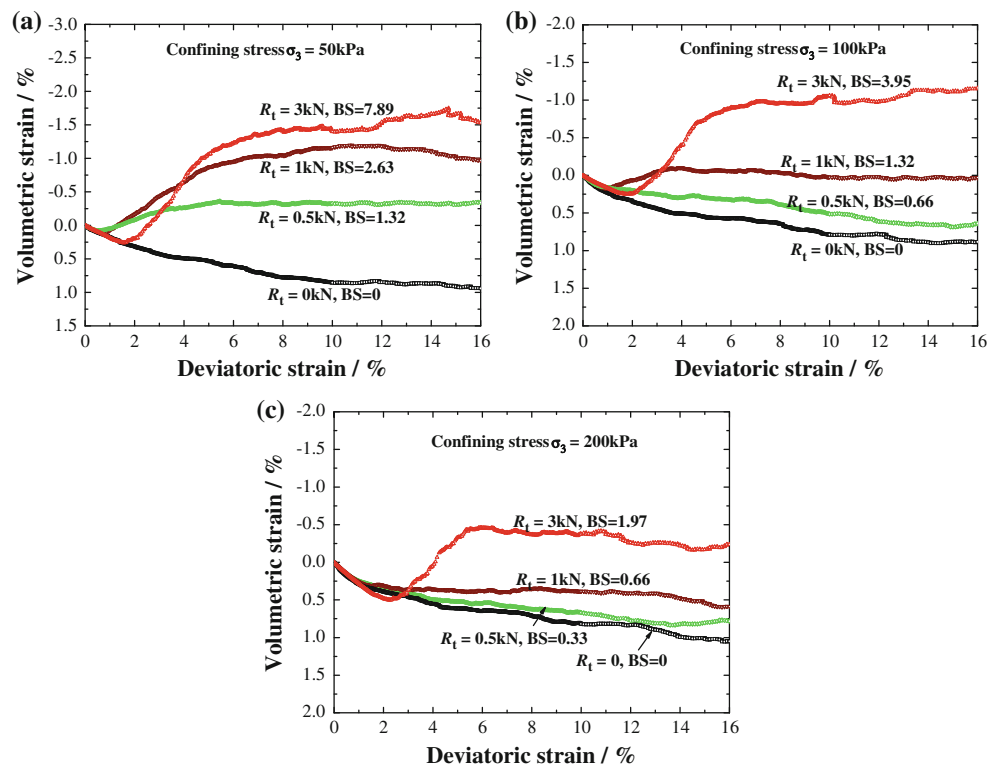


**Fig. 9** Volumetric responses of cemented granular materials for different bond strengths under different confining stress: **a**  $\sigma_3 = 50$  kPa; **b**  $\sigma_3 = 100$  kPa; **c**  $\sigma_3 = 200$  kPa

where,  $d\varepsilon_1$  and  $d\varepsilon_3$  represent the increment of the major and minor compressive strains respectively. From Fig. 10, a common trend of dilative behavior for all the cemented samples emerges whereby the dilation angle first increases to a peak value and then falls sharply to a constant near zero value. Moreover, the higher the bond strength is, the higher the dilation angle is. For instance, for tests run at 50 kPa of confinement, the maximum dilation angle varies from  $15^\circ$  (for  $R_t = 1$  kN) to  $28^\circ$  (for  $R_t = 3$  kN). The uncemented samples instead exhibit a compactive behavior.

#### 4.1.4 Bond strength models

Figure 11 shows the influence of the adopted bond strength curve (i.e.  $F_n - F_s$  plane) on the stress–strain response. The experimentally derived bond model is compared with two other models from the literature (see Fig. 11a): model 1, proposed by Jiang et al. [38], assumes a bond strength given by a frictional and cohesive contributions with the bond cohesion constant whatever the level of normal pressure; model 2 which is the standard bond model in PFC<sup>2D</sup> [27] assumes a constant (pressure independent) shear bond strength. In order to have a consistent comparison, the same value of tensile strength,  $R_t$ , was considered in all models.

It emerges that at low confinement (see Fig. 11b), there is little difference on the stress–strain response between the

three models. This is due to the fact that at low confinement, tension failure is dominant and the bond strength criteria differ little. However, at higher confinement (see Fig. 11c), it emerges that the peak deviatoric stress of the three models differ with the highest value related to model 1, the second to the experimentally derived bond model and the third to model 2. So we can conclude that the peak stresses are consistent with the bond strength of the models and the choice of the bond model is important. However, at high strains, no difference emerges since the residual strength assumed in all the three models is the same.

#### 4.2 Shear band formation

For sake of brevity, only one case ( $R_t = 3$  kN,  $\sigma_3 = 100$  kPa) was selected to illustrate the features of strain localization in the cemented granular materials. The test on cemented sample can be divided into five stages as indicated by points O and A–E, shown in Fig. 12. Point O stands for the initial state after isotropic consolidation. Point A can be seen as the initial yield point and marks the transition between contractive and dilative behaviors. Point B indicates the peak of the deviatoric stress and C the occurrence of maximum dilation. At point D, the deviatoric stress and volumetric strain keep almost constant. Finally, point E represents the end of the test. These points will be used to describe the features mentioned



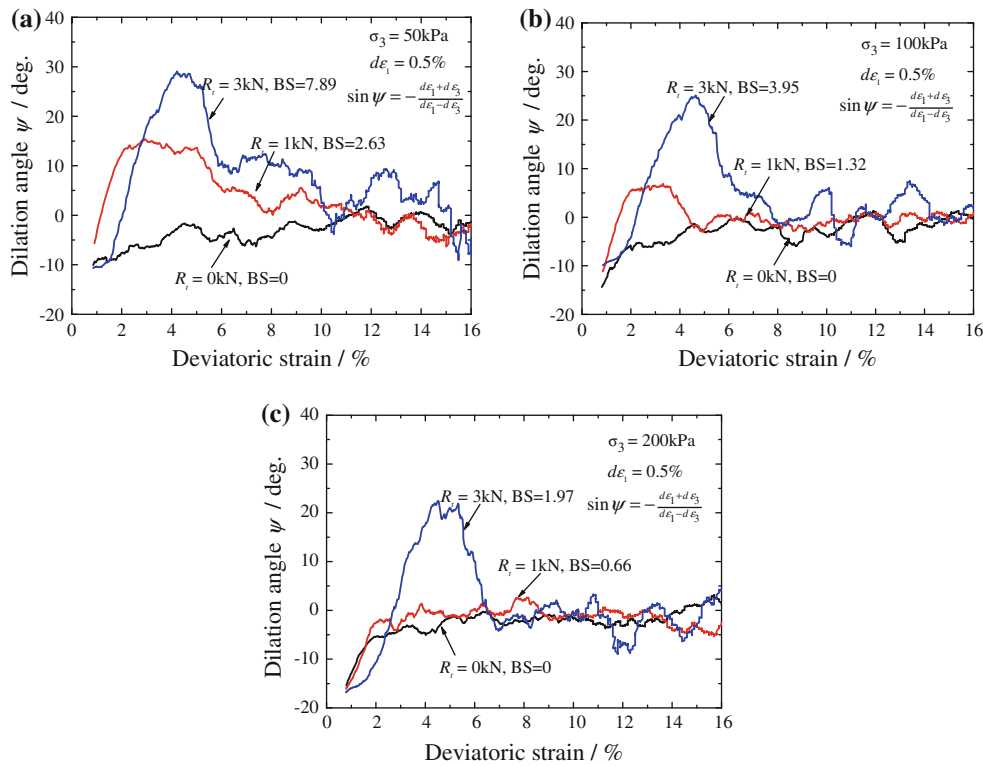


**Fig. 10** Dilation of samples with different values of bond strength under the following confining pressures: **a**  $\sigma_3 = 50 \text{ kPa}$ ; **b**  $\sigma_3 = 100 \text{ kPa}$ ; **c**  $\sigma_3 = 200 \text{ kPa}$

above of strain localization in the selected sample. The deviatoric strains at different loading stages are as follows: (A) 2.0%; (B) 3.2%; (C) 4.7%; (D) 12%; (E) 20%.

#### 4.2.1 Bonding breakage

It has been widely accepted that the shear bands in cemented granular materials are associated with bonding breakage (e.g., [19,38,46,66]). Figure 13 gives the relationship between spatial bonding breakage distribution and deviatoric strain. It can be seen that bonds remain intact at point A and begin to break in several narrow parallel bands shown as the blue dash line when the peak deviatoric stress is reached. With further increasing the deviatoric strain, the later broken bonds mainly concentrated in two of the narrow bands located in the bottom of the sample shown as the red full line. It is worth noting that the orientations of the narrow bands are among  $38\text{--}33^\circ$  with respect to the vertical which is the direction of the major principal stress. This range of values contains the value prescribed by the Coulomb’s orientation of shear failure (i.e.  $45^\circ - \varphi/2$ , where  $\varphi$  is the mobilized friction angle which is  $19.8^\circ$  in this case).

Further, Fig. 14 provides the bonding breakage ratio to present a more comprehensive study on the degradation of the microstructure. Here, the bonding breakage ratio  $r_{bf}$  is described as follows:

$$r_{bf} = \frac{N_{bf}}{N} \tag{8}$$

where,  $N_{bf}$  is the number of broken bonds and  $N$  the total number of bonds before isotropic consolidation.

It can be seen that within the shear band the bonding breakage ratio increases significantly from 6 to 50% with the average deviatoric strain going from 3 to 18%. Outside the shear bands instead, the bonding breakage ratio almost is zero regardless of the value of deviatoric strain.

A question may arise about the effect of the adopted grain shape (circular) on the observed bond breakage pattern. In fact, the shape here adopted is a simplification of the real grain shapes which tend to be irregular. Recently [11,24] ran DEM simulations on bonded grains of non-circular shapes. In particular [11] performed 2D biaxial DEM simulations on bonded polygonal particles which as in our case underwent progressive breakage under an increasing vertical load. In their simulations too, diagonal bands with concentrated bond breakages appear before failure of the sample. However, for lower load levels, when the first bonds in the sample start to break, in their simulations they appear scattered over the sample rather than concentrated along thin bands as in our case. This may be due to the particular shape of the adopted polygons and more simulations with various shapes would need to be run before drawing any general conclusion.

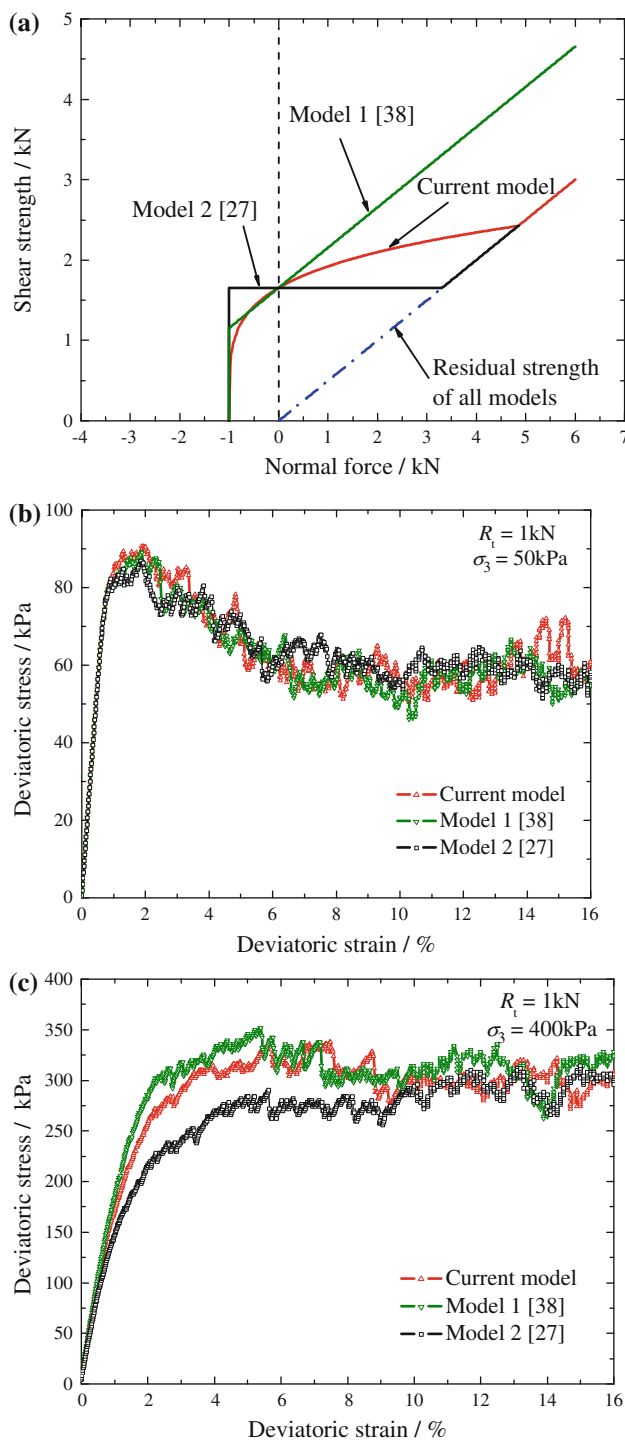


**Fig. 11** Comparison among three bond models: **a** shear strength of the models in the  $F_N$ – $F_S$  plane; **b** stress–strain relationship at low confinement; **c** stress–strain relationship at high confinement

Moreover, [11] employed only 1,000 particles in their simulations. According to our experience, at least 20,000 particles should be used to obtain repeatable patterns of behavior of the shear bands.

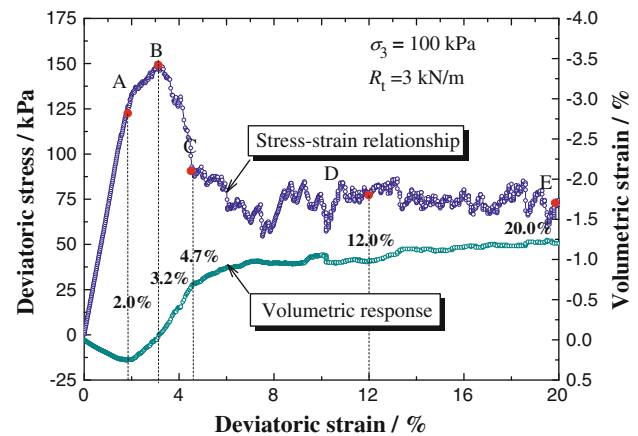


**Fig. 12** Mechanical response of selected case for analyzing strain localization

#### 4.2.2 Shear strain fields

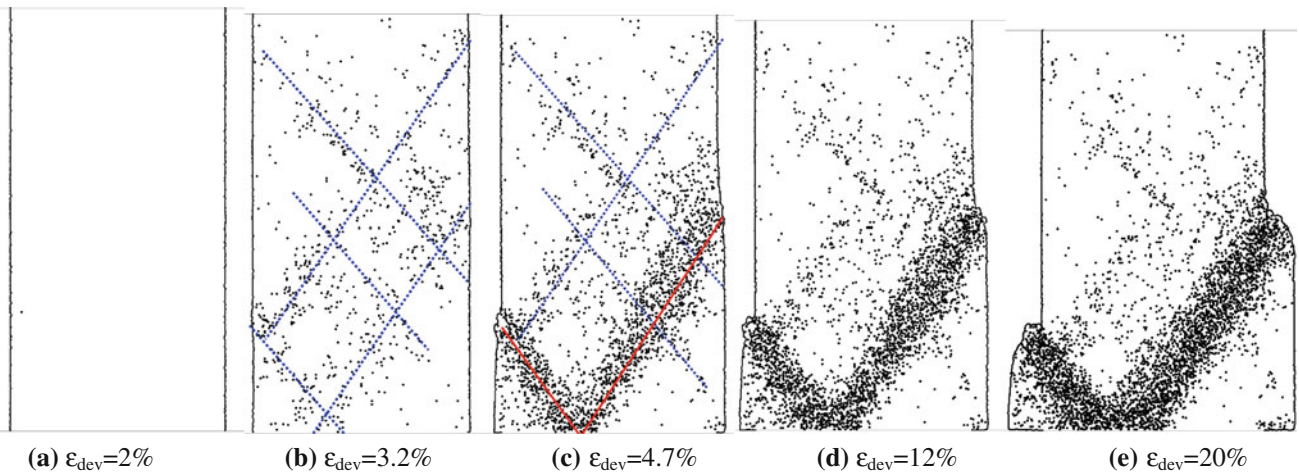
To measure local strains in the samples, mesh-free methods are often employed (e.g., [3,57,64,65]). In this study, we used a method recently proposed by Wang et al. [64] which in the calculation of the local strain field accounts for particle rotations and captures strain localization features with high resolution.

Figure 15 shows the field of shear strain at different loading stages. Clearly, two pronounced and concentrated shear bands are progressively shaped in the bottom of the cemented sample (Fig. 15a–e). The shear strain is mainly distributed in the transient shear bands at point B (Fig. 15b) and instead concentrated in the permanent shear bands after their formation (Fig. 15c–e). Furthermore, the shear bands turn thicker with increasing deviatoric strain (see Fig. 15c–e). Additionally, the shear behavior is distinctly restrained outside the shear band by the intact bonds. Compared with Figs. 14 and 15 implies that the evolution of shear strain is essentially related to bonding breakage. Consequently, the inclination of shear bands in cemented samples is seldom altered due to the uniform spatial distribution of bonding breakage.

#### 4.2.3 Principal stress vectors

In Fig. 16, the vectors indicating the direction of the principal stresses inside the sample are plotted for different loading stages. The black cross indicates the non-rotation major principal stress. In comparison, the blue and the red crosses mean the major principal stress rotate counterclockwise and clockwise respectively.

It can be seen that the directions of major principal stress remain vertical until the onset of the permanent shear bands, after that, the directions begin to rotate counterclockwise and



**Fig. 13** Distribution of bond breakage in cemented case at different loading stages corresponding to points **a–e** in Fig. 12

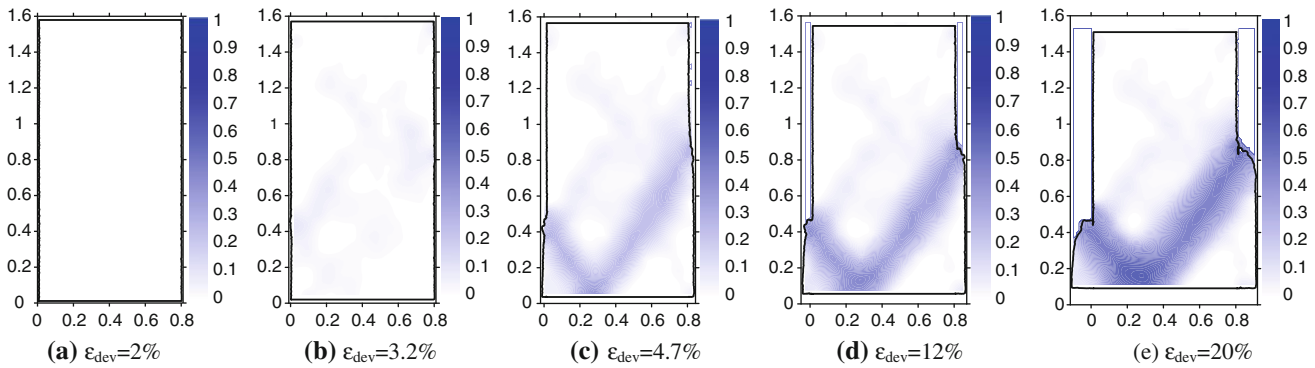


**Fig. 14** Distribution of bond breakage ratio in cemented case at different loading stages corresponding to points **a–e** in Fig. 12

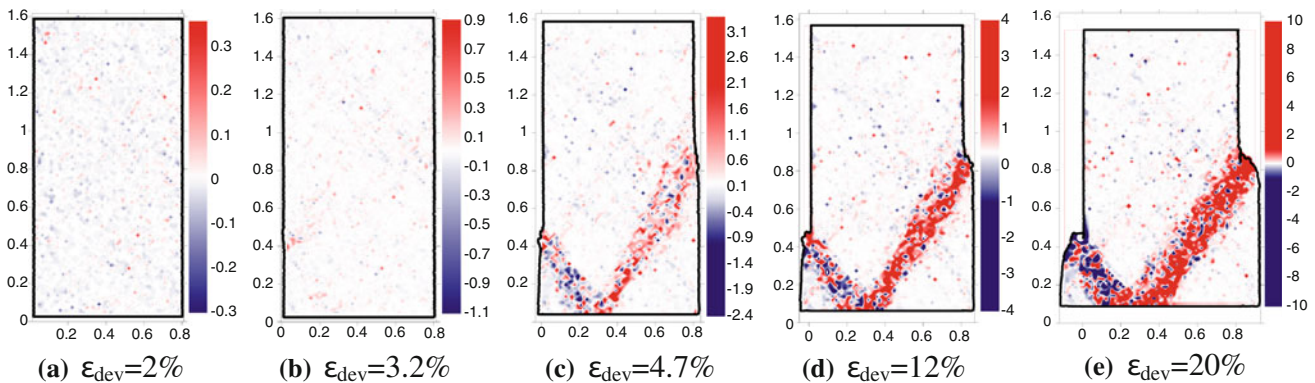


**Fig. 15** Distribution of shear strain in two cases at different loading stages corresponding to points **a–e** in Fig. 12

clockwise within the right and left shear bands respectively. In contrast, the stress vectors outside the shear band remain unchanged.

#### 4.2.4 APR distributions

Energy dissipation between sand particles may be proportional to the relative sliding displacement which can be

described by their sliding rotation rate. The sliding rotation rate, introduced in Jiang et al. [29], consists of two parts: one related to particle translation and the other to particle rotation and radius. The second part, hereafter called the pure rotation rate  $\dot{\theta}$ , can be computed by:

$$\dot{\theta} = \frac{1}{r}(r_1\dot{\theta}_1 + r_2\dot{\theta}_2) \tag{9}$$

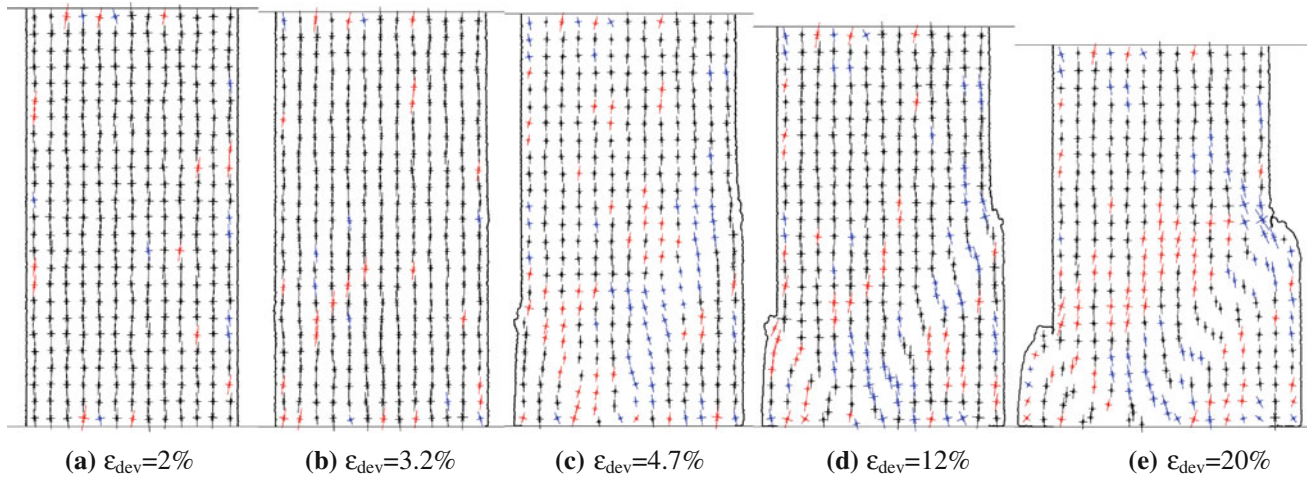


**Fig. 16** Principal stress vectors fields of two cases at different loading stages that corresponding to points **a–e** in Fig. 12

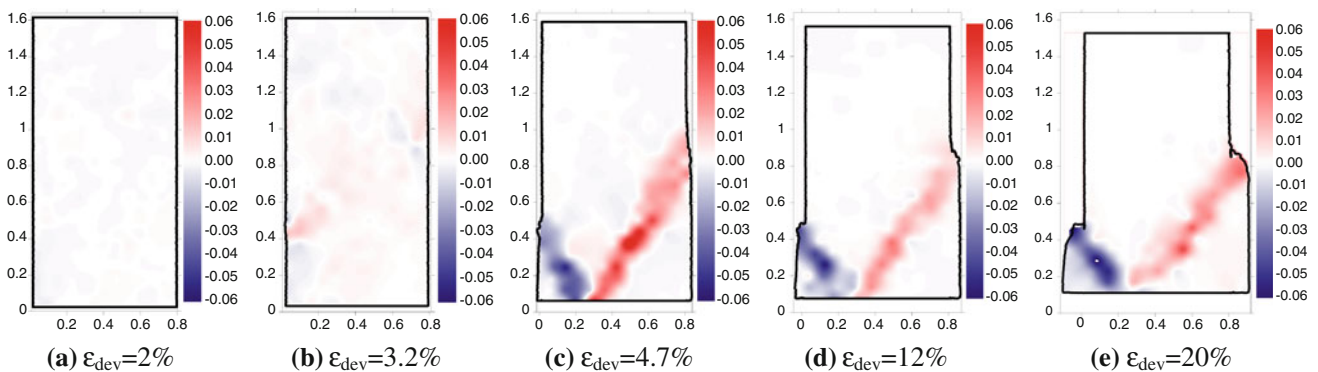


**Fig. 17** Distributions of averaged pure rotation rate (APR) of two cases at different loading stages that corresponding to points **a–e** in Fig. 12 (colour figure online)

where  $r_1$  and  $r_2$  are the radii,  $\hat{\theta}_1$  and  $\hat{\theta}_2$  are the rotation rates of two particles in contact.  $r$  is the equivalent radius of the two particles in contact, defined as:

$$r = \frac{2r_1r_2}{r_1 + r_2} \quad (10)$$

Therefore, the averaged pure rotation rate can be expressed by:

$$\omega = \frac{1}{N} \sum_{k=1}^N \hat{\theta} = \frac{1}{N} \sum_{k=1}^N \left[ \frac{1}{r^k} \left( \hat{\theta}_1^k r_1^k + \hat{\theta}_2^k r_2^k \right) \right] \quad (11)$$

where  $N$  is the total number of contacts and  $r^k$  is the equivalent radius for two particles in contact at the  $k$ th contact. Hence, APR is a local variable linking the macro- and micro-mechanics of sand motion which does not exist in classical continuum mechanics.

In Fig. 17 the fields of averaged pure rotation rate (APR) are plotted at various loading stages. The APR in the counter-clockwise direction is considered as positive (marked in red) whereas negative (marked in blue) in the clockwise direction. At small strains, the APR is homogeneously distributed

in the whole sample. However, at large strains, the APR is significantly concentrated in the shear bands with a positive and negative rotation inside the right and left shear bands respectively, clearly showing that particle rotation plays an important role in the formation of shear bands, which is consistent with the experimental results obtained by Oda [52].

#### 4.2.5 Microscopic behaviors inside and outside the shear bands

In Fig. 18, the main indicators of the development of shear bands (bonding breakage ratio and the shear strain, void ratio and averaged pure rotation rate) are presented with respect to the evolution of global deviatoric strain for the regions external and internal to the identified shear bands respectively. A total of eight circles (three along the left and five along the right shear bands) were used to calculate the values of the variables, see Fig. 18a. Each calculation circle has a radius of 75 mm, containing about 400 particles. It can be seen that the bonding breakage ratio, shear strain, void ratio and APR measured inside the shear band are much larger than the ones obtained outside the shear band after the peak devi-

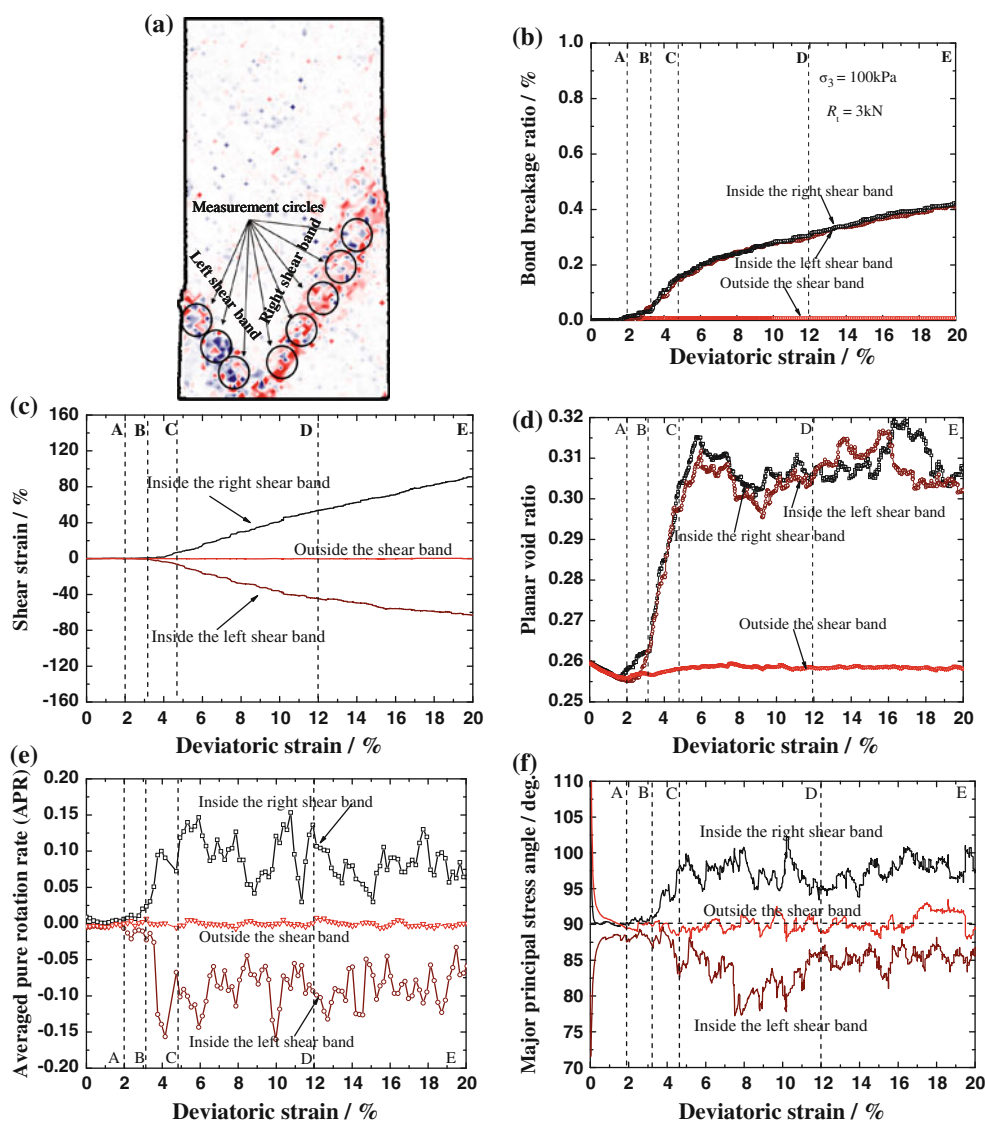


**Fig. 18** Relationships of local parameters and deviatoric strain observed inside and outside the shear bands for the cemented case: **a** Location of measurement circles; **b** bond breakage ratio; **c** shear strain; **d** planar void ratio; **e** APR; **f** inclination of the major principal stress

atoric stress is reached. For instance, the bonding breakage ratio (see Fig. 18b) is almost zero everywhere before point A. Then, it increases gradually (up to 40 %) inside the shear band while remains almost zero outside. Meanwhile, inside the shear bands, the direction of major principal stress strays away from the vertical direction around 5–10° after the occurrence of strain localization, shown in Fig. 18f. However, outside the shear bands, the angle of the major principal stress always fluctuates near the vertical direction at all stages.

Further, Fig. 19 provides the relationship between local deviatoric stress and strain both inside and outside the shear band. The local deviatoric stress and strain are measured from the measurement circles belonging to each zone, i.e. inside or outside the shear bands. Local strains can be expressed in terms of the first invariant of the strain tensor,  $\varepsilon_{ij}$ :

$$I_1 = \varepsilon_{ii} \tag{12}$$

and the second invariant of the strain deviator tensor:

$$I_2 = \frac{1}{2}(\varepsilon_{ii}\varepsilon_{jj} - \varepsilon_{ij}\varepsilon_{ij}) \tag{13}$$

As it can be expected, the local stress–strain relationship of the material inside the shear band is remarkably different from the relationship for the material outside (see Fig. 19). It emerges that the local deviatoric stress (both inside and outside the shear bands) sharply increase to a maximum value with  $I_1$  decreasing to a negative minimum value at initial stages where the shrinkage of the whole sample is evident. Then the local stress gradually drops to a low residual value with  $I_1$  slightly increasing to a value near zero outside the

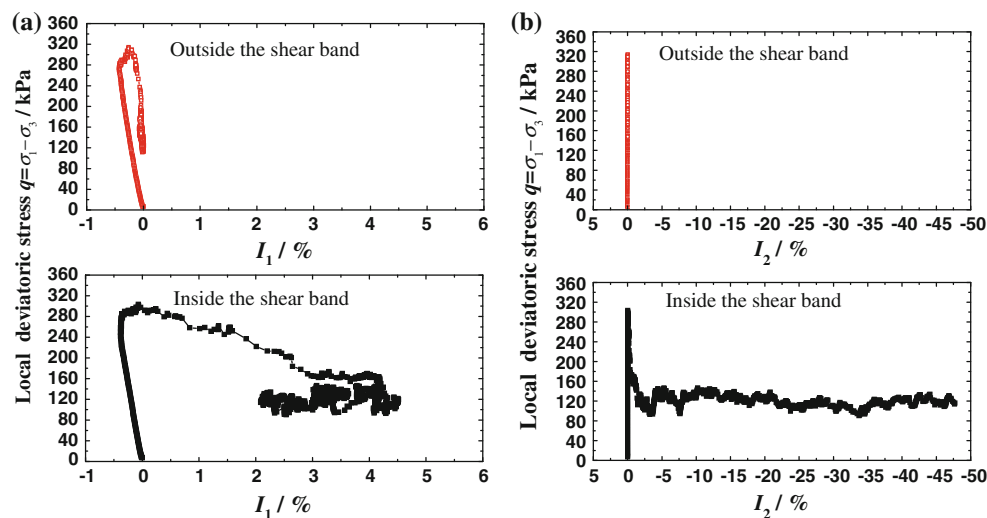


**Fig. 19** Relationships of local stress and strain observed inside and outside the shear bands for the cemented case: **a**  $q-I_1$  relationship; **b**  $q-I_2$  relationship

shear band and intensely rising to a constant positive value inside the shear band. Figure 19b shows that  $I_2$  is almost zero through the whole specimen before the peak deviatoric stress is reached. After that,  $I_2$  keeps increasing inside the shear band and remains constant outside. These responses indicate again that shear strain and dilation occur mainly inside the shear bands.

#### 4.3 Relationship between bond breakage and strain localization

It has been generally accepted that granular soils subjected to biaxial compression manifest strain localisation in several narrow zones which are generally called shear bands. From our simulations, it emerges that in case of a loose sample most of the bonds break up in tension as shown in Fig. 20a. In Fig. 20b, the rose diagrams illustrating the distributions of the directions of the bonds at the moment of breakage are shown. The rose diagrams were constructed by recording the normal orientation of bonds at breakage, and dividing the final data into 36 fractions each with an angle of  $10^\circ$ . It is interesting to note that bond breakages are strongly anisotropic. In particular, bonds break in tension in the horizontal direction (perpendicular to the major principal stress) whereas they break in shear along the orientations of the two conjugate shear bands.

##### 4.3.1 Effect of bond strength

In Fig. 21, the tensile and shear bond breakage ratios are plotted for various values of bond strength ( $R_t = 0.1, 0.5, 1$  and  $3$  kN) for tests run at  $100$  kPa of confining pressure. From Fig. 21a it emerges that the network of bonds is destroyed

quicker in case of low bond strength. For instance, nearly all the bonds are broken in case of a bond strength  $R_t = 0.1$  kN whereas  $90\%$  of bonds remain intact in case of  $R_t = 3$  kN. It can also be observed that at the beginning of the test in the case of  $R_t = 0.1$  kN, around  $60\%$  of bonds are broken, which shows that the microstructure in cemented granules at low bond strength can be seriously damaged already after the consolidation stage.

From Fig. 21b, c, it emerges that with decreasing the bond strength the predominant bond failure type changes from tensile type to shear type. In this figure, the tensile and shear bond breakage ratio,  $r_{tbf}$  and  $r_{sbf}$ , are defined as:

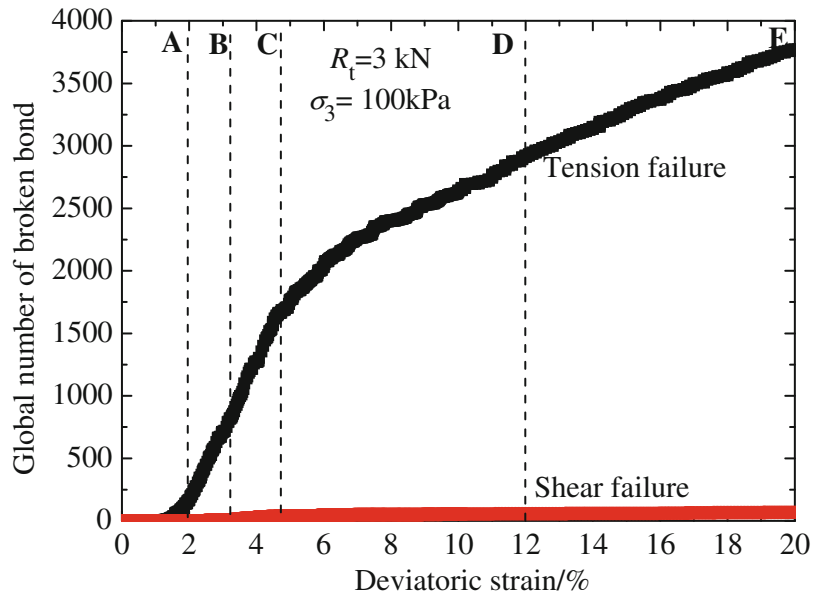
$$r_{tbf} = \frac{N_{tbf}}{N_{bf}}, \quad r_{sbf} = \frac{N_{sbf}}{N_{bf}} \quad (14a, b)$$

where  $N_{tbf}$  and  $N_{sbf}$  are the number of tensile and shear broken bonds respectively, and  $N_{bf}$  is the total number of broken bonds. Figure 22 further shows the spatial distributions of bond breakage ratio with various values of bond strength at  $12\%$  deviatoric strain.

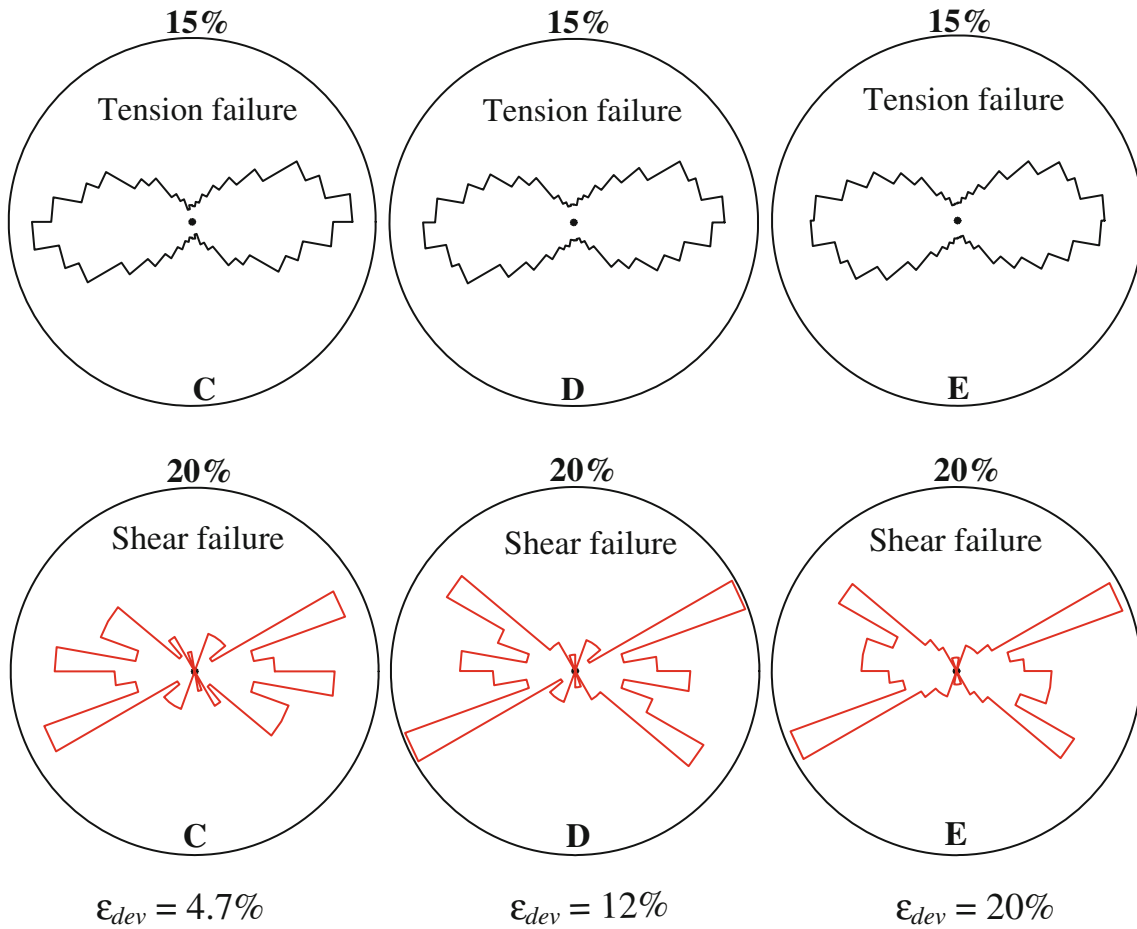
From the data in Figs. 21 and 22, two findings emerge: (1) at low bond strength, the shear strength of loose cemented granules mainly depends on the inter-particle friction, leading to a global shear failure (see Fig. 22a), this behavior is similar to the uncemented case; (2) it links the strain localization with the dominant tensile bond failure since they occur side by side in the strong cemented materials in our simulations (see Figs. 21b, 22).

##### 4.3.2 Effect of confining pressure

In Fig. 23a–c the total, tensile and shear bonding breakage ratios, respectively, are plotted against the deviatoric strain in



(a)



(b)

**Fig. 20** The global number and anisotropy of broken bonds both in tension failure and shear failure. **a** Number of bonds broker in tension and shear, **b** Anisotropy of bonds broken in tension and shear

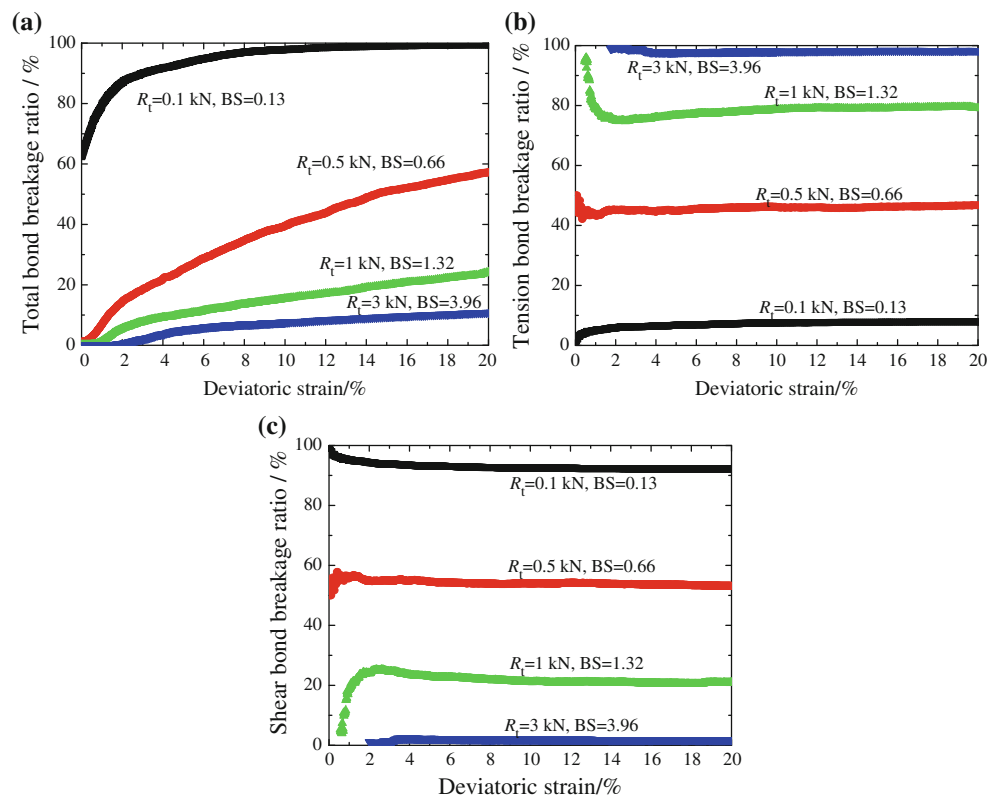


**Fig. 21** Tests for various bond strengths at  $\sigma_3 = 100$  kPa: **a** percentage of broken bonds over the total initial number of bonds; **b** percentage of bonds broken in tension; **c** percentage of bonds broken in shear

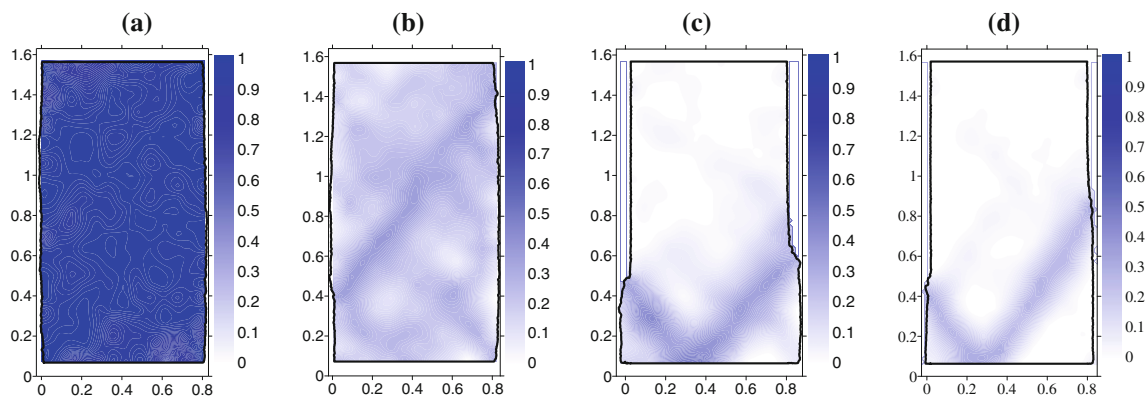


**Fig. 22** Distributions of bond breakage ratio for different values of bond strength ( $\sigma_3 = 100$  kPa): **a**  $R_t = 0.1$  kN ( $BS = 0.13$ ); **b**  $R_t = 0.5$  kN ( $BS = 0.66$ ); **c**  $R_t = 1$  kN ( $BS = 1.32$ ); **d**  $R_t = 3$  kN ( $BS = 3.96$ )

case of  $R_t = 1$  kN. Figure 24 further shows the bond breakage ratio distributions with various confining stresses at 12% of deviatoric strain. As it can be expected, the degradation of the bonds is quicker and more pronounced at high confinement than at low confinement, see Fig. 23a. The type of bond failure differs depending on the level of confinement. At low confining pressure (or high  $BS$ ), tensile bond failure is dominant and a high degree of strain localization takes place. At

high confining pressure (or low  $BS$ ), the shear bond failure is dominant with a low degree of strain localization taking place.

Concerning the effects of bond strength and confining pressure, two main features of strain localization for cemented granular materials have been revealed by the DEM simulations: (1) the higher the  $BS$  is, the higher the degree of strain localization exhibited; (2) strain localization is



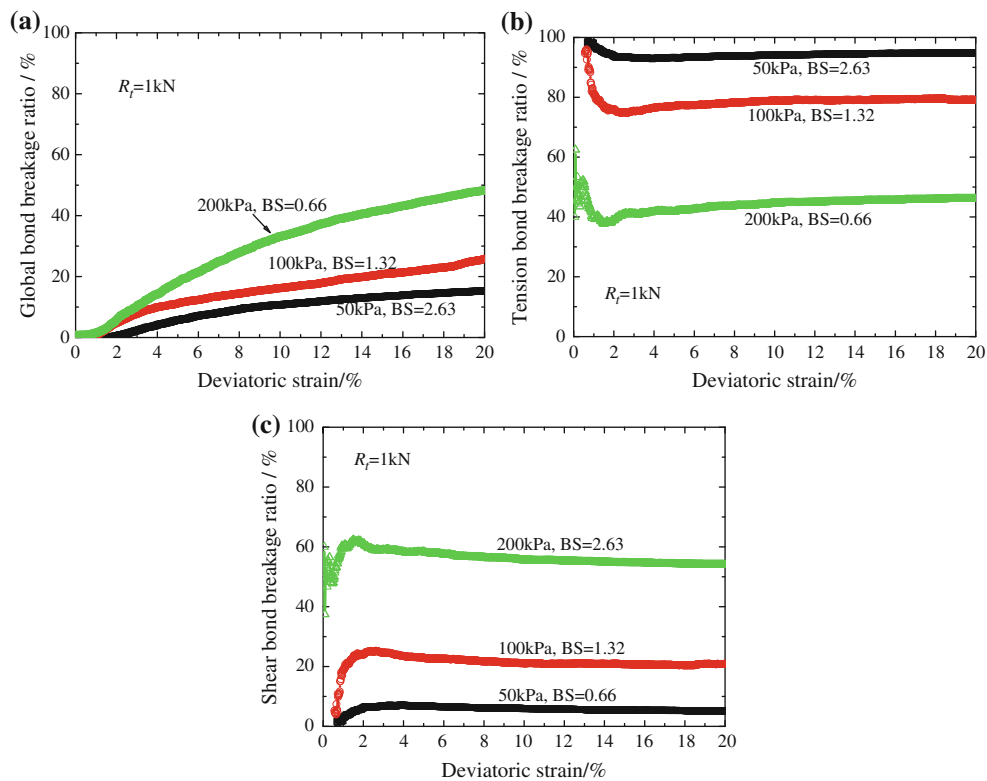


**Fig. 23** Tests at different confining pressures with  $R_t = 1 \text{ kN}$ : **a** percentage of broken bonds over the total initial number of bonds; **b** percentage of bonds broken in tension; **c** percentage of bonds broken in shear

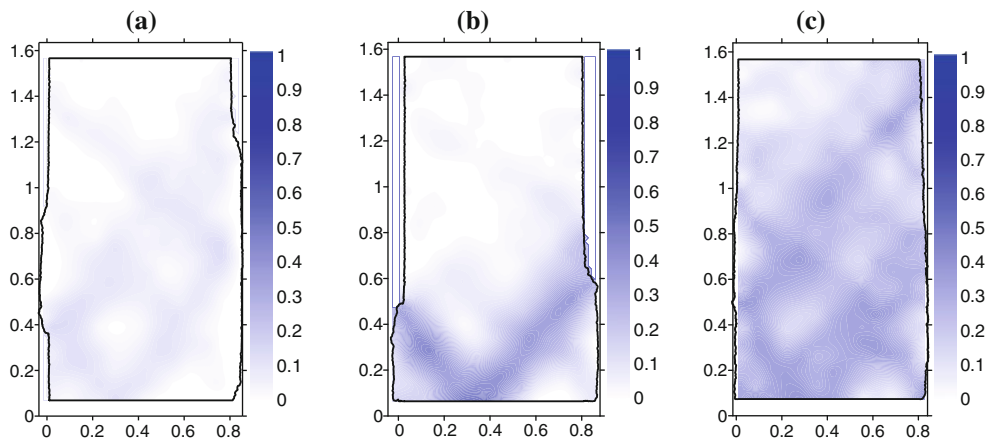


**Fig. 24** Distributions of bond breakage ratio for different confinement levels ( $R_t = 1 \text{ kN}$ ): **a**  $\sigma_3 = 50 \text{ kPa}$  ( $BS = 0.66$ ); **b**  $\sigma_3 = 100 \text{ kPa}$  ( $BS = 1.32$ ); **c**  $\sigma_3 = 200 \text{ kPa}$  ( $BS = 2.63$ )

commonly accompanied by tensile bond failure rather than shear one. This is mainly due to a strong dilation response during the occurrence of localization.

#### 4.4 Inclination and thickness of the shear bands

To further quantify the bonding effect on the strain localization, the two main features of shear bands, i.e. inclination

and thickness, are directly measured from the distribution of shear strain. From Fig. 13 it can be noted that the inclination of shear bands change little with increasing deviatoric strain. Hereafter, the observed shear band inclinations are compared with the inclinations predicted by three different theories according to: Coulomb,  $\vartheta_C$ , Roscoe [53],  $\vartheta_R$ , and Arthur–Vardoulakis [2,61],  $\vartheta_{AV}$ . Defining  $\vartheta_m$  as the angle of the band with the principal major stress direction, they are

**Table 2** Inclinations of shear bands for different values of bond strength and confinements

Bond strength $R_t$ , kN	$R_t = 0$			$R_t = 1$			$R_t = 3$		
	50	100	200	50	100	200	50	100	200
Confining pressure $\sigma_3$ , kPa									
Coloumb orientation, $\theta_C$	53°	53°	53°	52.3°	52.3°	52.3°	54.9°	54.9°	54.9°
Roscoe orientation, $\theta_R$	–	–	–	52.2°	48°	–	58.9°	57.2°	55.8°
Arthur–Vardoulakis orientation, $\theta_{AV}$	–	–	–	52.2°	50.1°	–	56.9°	56.1°	55.4°
Measured orientation, $\theta_m$	–	–	–	52°	53°	–	55°	55°	55°

**Table 3** Thicknesses of shear bands for different values of bond strength and confinements

	$R_t = 0$ kN	$R_t = 1$ kN	$R_t = 3$ kN
$\sigma_3 = 50$ kPa	–	17.1 $d_{50}$	12.4 $d_{50}$
$\sigma_3 = 100$ kPa	–	18.6 $d_{50}$	15.5 $d_{50}$
$\sigma_3 = 200$ kPa	–	–	16.8 $d_{50}$

given as follows:

$$\theta_C = 45 - \frac{\phi}{2} \quad (15)$$

$$\theta_R = 45 - \frac{\psi}{2} \quad (16)$$

$$\theta_{AV} = 45 - \frac{1}{2} \left( \frac{\phi + \psi}{2} \right) \quad (17)$$

where  $\phi$  and  $\psi$  are the mobilized friction and dilation angle respectively. The mobilized dilation angle was taken as the peak value from the curve in Fig. 10. In Table 2, the results are shown. The measured shear band inclination angle for cemented case with bond strength equaling to 1 kN/m is 52° and then it reaches 55° with increasing bond strength to 3 kN/m, showing a clear increase of  $\vartheta_m$  with  $R_t$  whereas little influence of the confining stress on  $\vartheta_m$  is observed. A further investigation suggests that the measured shear band orientations  $\vartheta_m$  are much closer to the Coulomb orientation.

In previous works the width of shear bands observed in biaxial tests was 8–20 times the median diameter  $d_{50}$  (e.g., [1, 18, 38, 50]). Hereafter, the width of the shear band is also normalized with respect to the median diameter  $d_{50}$  of the particles. In this study, the thickness is constructed by measuring the width along the direction perpendicular to the shear bands in the plots of the distributions of void ratio since the available experimental data of granular materials are mostly measured employing void ratio distributions. Table 3 gives the thickness variation in the samples with different values of bond strength and confining stress. The shear band thickness markedly decreases both with the bond strength and confining stress. It is obviously that the thickness of shear band at different conditions range from 12.4  $d_{50}$  to 18.6  $d_{50}$ , which

is in agreement with available experimental data. The results imply that bond degradation in cemented granular materials is restrained by relative high value of  $BS$ , and thus buckling of columns appears in a narrower zone.

## 5 Conclusions

In conclusion, by means of DEM analyses, we investigated the mechanical behavior and strain localization of loose cemented granular materials subjected to biaxial compression tests. An experimentally derived bond contact model [37] was employed for the first time. The effects of bond strength and confining pressure on the global stress–strain response and the dilation exhibited by the samples were investigated. Much attention of the paper was devoted to study the onset and development of shear bands inside the samples. Local stresses and strains inside and outside the shear bands were computed throughout the tests. The main conclusions of the study are summarized as follows:

1. The macro mechanical behavior of cemented granular material depends on both bond strength and confining pressure which can be incorporated into one dimensionless parameter, herein called the relative bond strength,  $BS$ . At low bond strength, or equivalently high confining stresses (i.e. low value of  $BS$ ), the cemented structure of samples is globally disrupted so that the material response approaches that of loose uncemented samples. In case of high relative bond strength ( $BS$ ) instead, samples exhibited strain softening and shear dilation, with bonds breaking mainly inside the shear band. The peak friction angle and cohesion exhibited by cemented samples increase with the level of bond strength. However, the peak friction angle of weak cemented granular materials is smaller than that of uncemented materials due to the fact that most bonds are intact at low confining pressure (i.e. high relative bond strength). The peak friction angle showed to increase with bond strength until becoming larger than the friction angle for the uncemented case. Also the residual friction angle showed to increase with increasing bond strength, but to a significantly less extent than the macroscopic cohesion and the peak friction angle. The increase of residual friction is likely due to the presence

of intact bonds inside the shear bands giving rise to non-negligible rolling resistance.

2. Shear band formation in cemented granular material is associated with gradual localization of bonding breakage, shear strain, rotation of stress vectors, void ratio and averaged pure rotation rate (APR). Bonding breakage ratio, shear strain, void ratio and APR measured inside the shear band are much larger than the values measured outside the shear band. The tensile bond failure rather than the shear failure is dominant within the shear bands.
3. The orientation of the shear bands for cemented samples varies largely with the level of bond strength. The measured orientations are in agreement with the orientations predicted by the classical Mohr–Coulomb criterion.
4. Shear band thickness showed to be dependent on the value of relative bond strength,  $BS$ : the higher the bond strength is, the thinner shear bands become; conversely the higher the confining pressure is, the thicker the shear bands become. The measured thicknesses for the bands varied from 12.4 to 18.6 of the median particle diameter  $d_{50}$ .

One of our future works is, based on the results of the current paper, to employ the DEM method to numerically investigate several boundary-value problems of cemented granulates in geotechnical engineering, such as: cone penetration tests (CPT) [30, 41, 44], tunnel lining [39], landslides [35, 60], cavity expansion [36].

**Acknowledgments** This research was financially supported by National Science Foundation of China for Distinguished Young Scientists with Grant No. 51025932, the Major Project of Chinese National Program for Fundamental Research and Development (973 Program) with Grant No. 2011CB013500, the Research Fund of the Doctoral Program of Higher Education with Grant No. 20100072110048, the EU FP7 IRSES “Geohazards and Geomechanics” with Grant No. 294976, and the Program for Changjiang Scholars and Innovative Research Team in University of China with Grant No. IRT1029. These supports are greatly appreciated.

## References

1. Alshibli, K.A., Hasan, A.: Spatial variation of void ratio and shear band thickness in sand using X-ray computed tomography. *Geotechnique* **58**(4), 249–257 (2008)
2. Arthur, J., Dunstan, T., Al-Ani, Q., Assadi, A.: Plastic deformation and failure in granular media. *Geotechnique* **27**(1), 53–74 (1977)
3. Bagi, K., Bojtár, I.: Different microstructure strain tensors for granular materials. In: Bicanic, N. (ed.) *Proceedings of the 4th International Conference on Analysis of Discontinuous Deformation*, pp. 261–271. University of Glasgow, UK (2001)
4. Brendel, L., Torok, J., Kirsch, R., Brockel, U.: A contact model for the yielding of caked granular materials. *Granul. Matter* **13**(6), 777–786 (2011)
5. Clough, G.W., Rad, N.S., Bachus, R.C., Sitar, N.: Cemented sands under static loading. *J. Geotech. Eng. (ASCE)* **107**(6), 799–818 (1981)
6. Consoli, N.C., Fonseca, A.V., Cruz, R.C., Heineck, K.S.: Fundamental parameters for the stiffness and strength control of artificially cemented sand. *J. Geotech. Geoenviron. Eng.* **135**(9), 1347–1353 (2009)
7. Consoli, N.C., Rotta, G.V., Prietto, P.D.M.: Yielding-compressibility-strength relationship for an artificially cemented soil cured under stress. *Geotechnique* **56**(1), 69–72 (2006)
8. Coop, M.R., Atkinson, J.H.: The mechanics of cemented carbonate sands. *Geotechnique* **43**(1), 53–67 (1993)
9. Cuccovillo, T., Coop, M.R.: Yielding and pre-failure deformation of structured sands. *Geotechnique* **47**(3), 491–508 (1997)
10. Cundall, P.A., Strack, O.L.: A discrete numerical model for granular assemblies. *Geotechnique* **29**(1), 47–65 (1979)
11. D’Addetta, G.A., Kun, F., Ramm, E.: On the application of a discrete model to the fracture process of cohesive granular materials. *Granul. Matter* **4**(2), 77–90 (2002)
12. Delenne, J.Y., Soulie, F., Youssoufi, M.S.E., Radjai, F.: From liquid to solid bonding in cohesive granular media. *Mech. Mater.* **43**(10), 529–537 (2011)
13. Delenne, J.Y., Topin, V., Radjai, F.: Failure of cemented granular materials under simple compression: experiments and numerical simulations. *Acta Mech.* **205**(1–4), 9–21 (2009)
14. Delenne, J.Y., Youssoufi, M.S.E., Cherblanc, F., Benet, J.C.: Mechanical behavior and failure of cohesive granular materials. *Int. J. Numer. Anal. Methods Geomech.* **28**(15), 1577–1594 (2004)
15. Desrues, J., Viggiani, G.: Strain localization in sand: an overview of the experimental results obtained in Grenoble using stereophotogrammetry. *Int. J. Numer. Anal. Methods Geomech.* **28**, 279–321 (2004)
16. Drescher, A., Vardoulakis, I.: Geometric softening in triaxial tests on granular material. *Geotechnique* **32**(4), 291–303 (1982)
17. Dupas, J.M., Pecker, A.: Static and dynamic properties of sand-cement. *J. Geotech. Eng. Div. ASCE* **105**(3), 419–436 (1979)
18. Estrada, N., Lizcano, A., Taboada, A.: Simulation of cemented granular materials: I. Macroscopic stress–strain response and strain localization. *Phys. Rev. E* **82**, 011303 (2010)
19. Estrada, N., Lizcano, A., Taboada, A.: Simulation of cemented granular materials: II. Micromechanical description and strength mobilization at the onset of macroscopic yielding. *Phys. Rev. E* **82**, 011304 (2010)
20. Haeri, S.M., Hamidi, A., Hosseini, S.M., Asghari, E., Toll, D.G.: Effect of cement type on the mechanical behavior of a gravely sand. *Geotech. Geol. Eng.* **24**(2), 335–360 (2006)
21. Haeri, S.M., Hosseini, S.M., Toll, D.G., Yasrebi, S.S.: The behavior of an artificially cemented sandy gravel. *J. Geotech. Geol. Eng.* **23**(5), 537–560 (2005)
22. Han, C.: *Localization of Deformation in Sand*. Ph.D. Thesis, University of Minnesota (1991)
23. Harris, W.W., Viggiani, G., Mooney, M.A., Finno, R.J.: Use of stereophotogrammetry to analyze the development of shear bands in sand. *Geotech. Test J. (ASTM)* **18**(4), 405–420 (1995)
24. Hidalgo, R.C., Kadau, D., Kanzaki, T., Herrmann, H.J.: Granular packings of cohesive elongated particles. *Granul. Matter* **14**(2), 191–196 (2012)
25. Huang, J.T., Airey, D.W.: Properties of artificially cemented carbonate sand. *J. Geotech. Geoenviron. Eng. (ASCE)* **124**(6), 492–499 (1998)
26. Ismail, M.A., Joer, H.A., Sim, W.H., Randolph, M.F.: Effect of cement type on shear behavior of cemented calcareous soil. *J. Geotech. Geoenviron. Eng. (ASCE)* **128**(6), 520–529 (2002)
27. Itasca Consulting Group Inc.: *Particle Flow Code in 2 Dimensions Version 4.0*. Minnesota (2008)
28. Iwashita, K., Oda, M.: Rolling resistance at contacts in simulation of shear band development by DEM. *J. Eng. Mech.* **124**(3), 285–292 (1998)

29. Jiang, M.J., Harris, D., Yu, H.S.: Kinematic models for non-coaxial granular materials. Part I: theory. *Int. J. Numer. Anal. Methods Geomech.* **29**, 643–661 (2005)
30. Jiang, M.J., Harris, D., Zhu, H.H.: Future continuum models for granular materials in penetration analyses. *Granul. Matter* **9**, 97–108 (2007)
31. Jiang, M.J., Konrad, J.M., Leroueil, S.: An efficient technique for generating homogeneous specimens for DEM studies. *Comput. Geotech.* **30**(7), 579–597 (2003)
32. Jiang, M.J., Leroueil, S., Konrad, J.M.: Insight into shear strength functions of unsaturated granulates by DEM analyses. *Comput. Geotech.* **31**, 473–489 (2003)
33. Jiang, M.J., Leroueil, S., Konrad, J.M.: Yielding of microstructured geomaterial by distinct element method analysis. *J. Eng. Mech. (ASCE)* **131**(11), 1209–1213 (2005)
34. Jiang, M.J., Zhu, H.H., Li, X.M.: Strain localization analyses of idealized sands in biaxial tests by distinct element method. *Front. Architect. Civil Eng. China (FAC)* **4**(2), 208–222 (2010)
35. Jiang, M.J., Murakami, A.: Distinct element method analyses of idealized bonded-granulate cut slope. *Granul. Matter* **14**, 393–410 (2012)
36. Jiang, M.J., Sun, Y.G.: Cavity expansion analyses of crushable granular materials with state-dependent dilatancy. *Int. J. Numer. Anal. Methods Geomech.* **36**, 723–742 (2012)
37. Jiang, M.J., Sun, Y.G., Li, L.Q., Zhu, H.H.: Contact behavior of idealized granules bonded in different interparticle distances: an experimental investigation. *Mech. Mater.* **55**, 1–15 (2012)
38. Jiang, M.J., Yan, H.B., Zhu, H.H., Utili, S.: Modeling shear behavior and strain localization in cemented sands by two-dimensional distinct element method analyses. *Comput. Geotech.* **38**(1), 14–29 (2011)
39. Jiang, M.J., Yin, Z.Y.: Analysis of stress redistribution in soil and earth pressure on tunnel lining using the discrete element method. *Tunn. Undergr. Space Technol.* doi:[10.1016/j.tbr.2011.03.031](https://doi.org/10.1016/j.tbr.2011.03.031) (2012)
40. Jiang, M.J., Yu, H.S., Harris, D.: Bond rolling resistance and its effect on yielding of bonded granulates by DEM analyses. *Int. J. Numer. Anal. Methods Geomech.* **30**(7), 723–761 (2006)
41. Jiang, M.J., Yu, H.S., Harris, D.: Discrete element modeling of deep penetration in granular soils. *Int. J. Numer. Anal. Methods Geomech.* **30**(4), 335–361 (2006)
42. Jiang, M.J., Yu, H.S., Leroueil, S.: A simple and efficient approach to capturing bonding effect in naturally-microstructured sands by discrete element method. *Int. J. Numer. Methods Eng.* **69**, 1158–1193 (2007)
43. Jiang, M.J., Zhu, H.H.: An interpretation of the internal length in Chang's couple-stress continuum for bonded granulates. *Granul. Matter* **9**, 431–437 (2007)
44. Jiang, M.J., Zhu, H.H., Harris, D.: Classical and non-classical kinematic fields of two-dimensional penetration tests on granular ground by discrete element method analyses. *Granul. Matter* **10**, 439–455 (2008)
45. Khun, M.R.: A flexible boundary for three-dimensional DEM particle assemblies. *Eng. Comput.* **12**, 175–183 (1995)
46. Leroueil, S., Vaughan, P.R.: The general and congruent effects of structure in natural soils and weak rocks. *Geotechnique* **40**(3), 467–488 (1990)
47. Luding, S., Alonso-Marroquin, F.: The critical-state yield stress (termination locus) of adhesive powders from a single numerical experiment. *Granul. Matter* **13**(2), 109–119 (2011)
48. Mandel, J.: Conditions de stabilité et postulat de Drucker. In: *Proceedings of IUTAM Symposium on Rheology and Soil Mechanics*, pp. 58–68 (1966)
49. Mansouri, M., Delenne, J.Y., Seridi, A., Youssoufi, M.S.E.: Numerical model for the computation of permeability of a cemented granular material. *Powder Technol.* **208**(2), 532–536 (2011)
50. Muhlhaus, H.B., Vardoulakis, I.: The thickness of shear bands in granular materials. *Geotechnique* **37**(3), 271–283 (1987)
51. Nemat-Nasser, S., Okada, N.: Radiographic and microscopic observation of shear bands in granular materials. *Geotechnique* **51**(9), 753–765 (2001)
52. Oda, M., Konishi, J., Nemat-Nasser, S.: Experimental micromechanical evolution of strength of granular materials: effects of particle rolling. *Mech. Mater.* **1**(4), 269–283 (1982)
53. Roscoe, K.H.: The influence of strains in soil mechanics. Tenth Rankine Lecture, *Geotechnique* **20**(2), 129–170 (1970)
54. Rotta, G.V., Consoli, N.C., Prietto, P.D.M., Coop, M.R., Graham, J.: Isotropic yielding in an artificially cemented soil cured under stress. *Geotechnique* **53**(5), 493–501 (2003)
55. Saxena, S.K., Lastrico, R.M.: Static properties of lightly cemented sand. *J. Geotech. Eng. Div. (ASCE)* **104**(12), 1449–1465 (1978)
56. Stegmann, T., Torok, J., Brendel, L., Wolf, D.E.: Minimal dissipation theory and shear bands in biaxial tests. *Granul. Matter* **13**(5), 565–572 (2011)
57. Thomas, P.A.: *Discontinuous Deformation Analysis of Particulate Media*. Ph.D. Thesis, Department of Civil Engineering, University of California, Berkeley (1997)
58. Thornton, C., Zhang, L.: A numerical examination of shear banding and simple shear non-coaxial flow rules. *Philos. Mag.* **86**(21–22), 3425–3452 (2006)
59. Utili, S., Nova, R.: DEM analysis of bonded granular geomaterials. *Int. J. Numer. Anal. Methods Geomech.* **32**, 1997–2031 (2008)
60. Utili, S., Crosta, G.B.: Modelling the evolution of natural cliffs subject to weathering: 2. Discrete element approach. *J. Geophys. Res.* **116**, F01017 (2011)
61. Vardoulakis, I.: Shear band inclination and shear modulus of sand in biaxial tests. *Int. J. Numer. Anal. Methods Geomech.* **4**(2), 103–119 (1980)
62. Vermeer, P.A.: The orientation of shear bands in biaxial tests. *Geotechnique* **40**(2), 223–236 (1990)
63. Viggiani, G., Lenoir, N., Besuelle, P., Di-Michiel, M., Marello, S., Desrues, J., Kretschmer, M.: X-ray microtomography for studying localized deformation in fine-grained geomaterials under triaxial compression. *C. R. Mec.* **332**(10), 819–826 (2004)
64. Wang, J.F., Gutierrez, M.S., Dove, J.E.: Numerical studies of shear banding in interface shear tests using a new strain calculation method. *Int. J. Numer. Anal. Methods Geomech.* **31**(12), 1349–1366 (2007)
65. Wang, J.F., Jiang, M.J.: Unified soil behavior of interface shear test and direct shear test under the influence of lower moving boundaries. *Granul. Matter* **13**(5), 631–641 (2011)
66. Wang, Y.H., Leung, S.C.: A particular-scale investigation of cemented sand behavior. *Can. Geotech. J.* **45**(1), 29–44 (2008)
67. Wang, Y.H., Leung, S.C.: Characterization of cemented sand by experimental and numerical investigations. *J. Geotech. Geoenviron. Eng. (ASCE)* **134**(7), 992–1004 (2008)
68. White, D.J., Take, W.A., Bolton, M.D.: Soil deformation measurement using particle image velocimetry (PIV) and photogrammetry. *Geotechnique* **53**(7), 619–631 (2003)
69. Yan, W.M., Li, X.S.: A model for natural soil with bonds. *Geotechnique* **61**(2), 95–106 (2011)
70. Yu, H.S., Tan, S.M., Schnaid, F.: A critical state framework for modelling bonded geomaterials. *Geomech. Geoeng.* **2**(1), 61–74 (2007)
71. Yun, T.S., Evans, T.M.: Evolution of at-rest lateral stress for cemented sands: experimental and numerical investigation. *Granul. Matter* **13**, 671–683 (2011)
72. Zeghal, M., Shamy, U.E.I.: Liquefaction of saturated loose and cemented granular soils. *Powder Technol.* **184**, 254–265 (2008)